Diploma Thesis

Studying piezoelectric excitation of hierarchically structured materials by means of multiscale modeling

submitted for acquiring the academic degree
"Diplom-Ingenieur" (equivalent to Master of Science)
at the Vienna University of Technology, Faculty of Civil Engineering

---

Diplomarbeit

Untersuchung piezoelektrischer Anregung von hierarchisch strukturierten Gewebe mittels Multiskalenmodellierung

eingereicht zur Erlangung des akademischen Grades „Diplom-Ingenieur"
an der Technischen Universität Wien, Fakultät für Bauingenieurwesen

von

Erik Kornfellner, BSc

Matr.Nr.: 01528987

unter der Anleitung von

Associate Prof. Dipl.-Ing. Dr.techn. **Stefan Scheiner**

Institut für Mechanik der Werkstoffe und Strukturen
Forschungsbereich Festigkeitslehre und Biomechanik
Technische Universität Wien
Karlsplatz 13/E202, 1040 Wien, Österreich

Wien, im Sommersemester 2020 _____

Abstract

Bone tissue is known to possess piezoelectric properties, owing to the respective behavior of some of bone constituents. In the past, piezoelectric excitation has been suggested to be one of the mechanisms involved in mechanical stimulation of the bone cell activities involved in bone remodeling. However, due to the very small length scales on which the related processes occur it is not possible to study the role of bone piezoelectricity for bone remodeling based on experiments. This thesis investigates this potentially important process by means of multiscale modeling.

In particular, the fundamental concept of continuum micromechanics was extended such that the well-known equations for stiffness homogenization could be extended to upscaling the so-called electromechanical tensor, comprising stiffness as well as electrical quantities. In further consequence, this concept allows for downscaling macroscopically applied mechanical loading to microscopically experienced electrical stimuli. Applying this mathematical framework to the previously established multiscale micromechanical representation of bone tissue has shown that the electrical stimuli arriving, in response to physiological macroscopic loading, at the level of bone cells is much too small to play a significant role in mechanical stimulation of bone cell activities. Furthermore, sensitivity studies as to specific morphological features of bone tissue, as well as to the effect of deformation were studied. Essentially, the results of this study show that mechanical stimulation of bone cells is most likely caused by other mechanisms, such as the pressurization of bone cells due to macroscopic loading.

In addition, the new multiscale method was applied to the tissues making up teeth, enamel and dentin. Particularly for the elasticity properties, the model predictions agree very well with corresponding experimental data, hence yielding new homogenization schemes for enamel and dentin as remarkable side products of this thesis.

Kurzfassung

Es ist wohlbekannt, dass Knochengewebe piezoelektrische Eigenschaften aufweist, aufgrund des entsprechenden Verhaltens auf der Ebene der Knochenbestandteile. In Studien zur Anregung von Zellaktivitäten im Knochengewebe durch mechanische Belastung wurde die mögliche Rolle der piezoelektrischen Aktivierung von Zellen mehrfach genannt. Da die entsprechenden Prozesse auf sehr kleinen Längenskalen ablaufen, ist eine experimentelle Untersuchung allerdings nicht möglich. Ziel dieser Diplomarbeit war die Ergründung der Rolle piezoelektrischer Anregung von Zellaktivitäten im Knochengewebe mittels Multiskalenmodellierung.

Zu diesem Zweck wurde das grundlegende Konzept der Kontinuumsmikromechanik substanziell erweitert, sodass die im Rahmen dieses Konzepts etablierten Homogenisierungsschemen nicht nur die elastischen Eigenschaften berücksichtigen, sondern auch die relevanten elektrischen Größen. In weiterer Folge kann dadurch auch die makroskopisch aufgebrachte mechanische Belastung hinsichtlich der entsprechend auftretenden elektrischen Stimuli auf mikroskopischer Ebene interpretiert werden. Diese Modellierungsstrategie wurde dann auf ein bereits etablierte Mehrskalenmodell von Knochengewebe angewendet. Es konnte gezeigt werden, dass die durch physiologische makroskopische Belastung hervorgerufenen elektrischen Stimuli auf Zellebene deutlich zu klein sind um eine effektive Stimulierung der Zellen zu erreichen. Des Weiteren wurden Sensitivitätsstudien durchgeführt, um die Relevanz von morphologischen Kenngrößen sowie den Effekt von Deformationen zu quantifizieren. Insgesamt zeigen die erzielten Ergebnisse, dass für die mechanische Stimulierung von Knochenzellen höchstwahrscheinlich andere Mechanismen verantwortlich sind, wie z.B. der hydrostatische Druck, der auf Knochenzellen wirkt.

Zusätzlich wurde die vorgestellte Multiskalenmethode auf jene Gewebe, aus denen Zähne bestehen, Zahnschmelz und Dentin, angewendet. Hier zeigen sich insbesondere bei den elastischen Eigenschaften gute Übereinstimmungen von Modellvorhersagen und experimentellen Daten. Folglich sind die Homogenisierungsschemen, welche für Zahnschmelz und Dentin formuliert wurden, als bemerkenswerte Nebenprodukte dieser Diplomarbeit zu betrachten.

Contents

1 Introduction

Since Julius Wolff investigated the changes of bone after a trauma or changed use at the end of the 19^{th} century, we know that bone in a living organism is steadily altering and adapting to changed loading conditions [1]. Little was known at this time, what mechanism controls the permanent processes of dismantling and constructing new bone material.

Function and behavior of bone material

The rigid bone structure has many functions in the body like Haematopoiesis [2], the building of new blood cells, as some endocrine functions [3] and is used as a reservoir for minerals. But the most apparent use of bone is its mechanical structure, whether it is used as a protection for the internal organs or for body movements together with the attached muscles.

Bone is composed from the extracellular matrix, which gives the organ its structure and stability, and osteocytes, bone cells which lie embedded in the extracellular matrix and maintain this cell-less matrix. More specialized cells can be found in the bone, like the big multinucleated osteoclasts, which keep breaking down the extracellular matrix and process the gained minerals, or osteoblasts, which build new bone matrix by depositing hydroxyapatite and collagen, which are the main building blocks of the extracellular matrix.

Use of this regulation is to adapt the bone material to the required strength. Similar to an athlete whose muscles get stronger, when he is weightlifting, the bones also need to become stronger to hold heavier loads. On the other hand, if the bone is no longer required to carry any weight, like it is the case for paralyzed people or the tight bone of a wheelchair driver, the bone matrix will become less dense and its stability will decrease. The same effect occurs, when a joint is replaced by an endoprosthesis. When the prosthesis is fixed with a long shaft in the bone, the much more rigid shaft, usually made of metal, will shield the bone around from mechanical stress, resulting in a weakening of the affected bone material.

Since these effects have been discovered, many attempts were made to find out, how osteocytes are able to recognize mechanical load and share this information, to adapt the surrounding bone material. At this point, many possibilities are acquainted, to

how cells can interact with their surroundings, may it be membrane elements, which depend on voltage, chemical stimuli or mechanical strain.

Relevant preceding studies on bone material

More recent researches show that bone processes not only react with various chemical stimuli, but bone cells are also able to transfer this information to other osteocytes [4]. Other experiments, where bone was exposed to ultrasound, demonstrated that bone adapts to mechanical stimuli, still not able to pinpoint the exact mechanisms which cause these effects [5]. Some models already describe piezoelectric effects [6], a material characteristic to cause electric polarization when under mechanical strain, and more specific simulations indicate bone cell activity caused by stress from fluids [7]. Further, in-vitro studies with unhinged bone cells showed, that bone cells are also able to interact with the extracellular matrix and might use it to propagate signals, impacting the growth and morphology of the osteocytes [8]–[10].

Knowledge of the bone growing behavior might be useful for creating bone healing supplies, curing fractures and traumas, since the healing process of bone takes long and does not always result in fully functional tissue [11]. Better understanding of these natural processes might also influence training methods for athletes or ways to keep astronauts fit, who suffer from bone atrophy in zero gravity [12].

Intent of this thesis

Facing the various propositions of signaling pathways, and assuming that there is likely more than a single mechanism involved, the question arises, if osteocytes are affected directly by the extracellular matrix, through its piezoelectric effect. Starting point of this consideration, is a humans everyday locomotion, causing in example the thigh bone to bend, every time the body weight is put on this leg. Due to the bones piezoelectric properties, an electrical polarization might impact the osteocytes corresponding to the inflicted strain.

It is well known that most cells in the human body can interact via polarization of their cell membrane. Further it is known, that bone possesses piezoelectric properties, as well as its main building materials, namely collagen and hydroxyapatite crystals. For the macroscopic bone material, as well as for the microscopic building blocks the material properties have been measured and identified. However none of these size scales match the length of a typical bone cell, so it is rather unfavorable to examine one of these material properties in respect of bone cells.

The idea is to find a procedure to calculate the occurring material phases in bone and evaluate their corresponding length scales. With these properties known it might be

possible to make a statement whether bone cells are affected by piezoelectric effects from the extracellular bone structures or not.

Of course the question arises what the effect of the exact material geometry is, or how big the impact of the simplification is. By disregarding some material minorities the macroscopic properties might change, therefore it is useful to investigate how a simulation of the material properties is affected by changing geometries and composition of its building blocks.

Structure of this thesis

This document is about estimating material properties for the different size scales from its basic building blocks to a macroscopic bone material, which we can compare to measured material properties. It further examines material phases at the size of bone cells and their effect on them. But before, the mixing scheme to homogenize material phases is introduced and validated by measurement values of macroscopic structures, as well as some possibilities and applications of this estimation concept are shown.

It may be mentioned at this point, that this hierarchical structure applies not exclusively to bone. Many other structures like concrete and wood can be estimated with similar approaches. Especially dentin and enamel, which can be found in the human tooth, are investigated in this work, since they are built from the same materials as bone and are also known to show piezoelectric properties.

Therefore this work will start with the required mathematical notation, before introducing the theory of continuum mechanics to homogenize material structures and explain how the required Piezo-Eshelby tensor can be derived. In chapter 5 the earlier introduced methods will be applied to bone material and the piezoelectric impact will be discussed thereafter.

In the subsequent chapters, the possibilities of the homogenization concept will be pictured, how various volume fractions and different inclusion geometries can affect the simulation. Ultimately the concept will be transferred from bone to other materials, namely tooth enamel and dentin, and the simulation will be applied to different structures and material compositions.

2 Fundamentals of the theory

In order to find a context between the macroscopic properties and its elementary building blocks, it is necessary to define the properties of a specific material for its respective spatial size scale. To do so, the material will be handled as a continuum at the observed scale.

2.1 Basic concepts of continuum micromechanics

Continuum mechanics forgo individual particles in a material compound and treat it as a homogeneous mass, although the existence of inhomogeneities is known. The material has to be observed as a representative volume Element - *RVE*, whereby the selection of the size scale is crucial, since the included inhomogeneities have to be significantly smaller than the observed area, which itself has to be much smaller than the next bigger structure the material is contributing to.

Thus, the benefit of achieving a continuous material, where every subsection has the same properties as the bulk material, goes with the constraint that only material phases with clearly separated size scales can be handled. The estimation of the material properties when building a bigger structure from multiple smaller material phases will be referred to as *homogenization*.

2.2 Voigt and Kelvin-Mandel notation

For the following calculations, the elastic c, piezoelectric e and dielectric κ properties of a material are needed. While stiffness is usually defined as a fourth-order tensor and piezoelectricity as a third-order tensor, it is useful to introduce the electromechanical coupling moduli $\mathbb{M}$, a fourth-order tensor, which is a combination of c, e, κ, and allows us to calculate all parameters in one step, if written as a second-order tensor $\mathbf{M}$ [13].

To reduce mathematical complexity, calculations of tensors higher than rank 2 can be obviated by utilizing the material symmetries and applying Voigt notation. This results in the way easier representation for the electromechanical coupling moduli $\mathbf{M}$, as in Equation 2.1.

$$\mathbf{M}_{voigt} = \begin{pmatrix} c_{11} & c_{12} & c_{13} & c_{14} & c_{15} & c_{16} & e_{11} & e_{21} & e_{31} \\ c_{21} & c_{22} & c_{23} & c_{24} & c_{25} & c_{26} & e_{12} & e_{22} & e_{32} \\ c_{31} & c_{32} & c_{33} & c_{34} & c_{35} & c_{36} & e_{13} & e_{23} & e_{33} \\ c_{41} & c_{42} & c_{43} & c_{44} & c_{45} & c_{46} & e_{14} & e_{24} & e_{34} \\ c_{51} & c_{52} & c_{53} & c_{54} & c_{55} & c_{56} & e_{15} & e_{25} & e_{35} \\ c_{61} & c_{62} & c_{63} & c_{64} & c_{65} & c_{66} & e_{16} & e_{26} & e_{36} \\ e_{11} & e_{12} & e_{13} & e_{14} & e_{15} & e_{16} & -\kappa_{11} & -\kappa_{12} & -\kappa_{13} \\ e_{21} & e_{22} & e_{23} & e_{24} & e_{25} & e_{26} & -\kappa_{21} & -\kappa_{22} & -\kappa_{23} \\ e_{31} & e_{32} & e_{33} & e_{34} & e_{35} & e_{36} & -\kappa_{31} & -\kappa_{33} & -\kappa_{33} \end{pmatrix} \tag{2.1}$$

Since the mechanical stress σ and strain ε, which corresponds to the elasticity c, can be written as a first-order tensor instead of a second-order tensor, to match the matrix notation of the elasticity matrix, it is useful to write the electromechanical coupling moduli $\mathbf{M}$ in Kelvin-Mandel notation, as in Equation 2.2.

$$\mathbf{M}_{kelvin-mandel} = \begin{pmatrix} c_{11} & c_{12} & c_{13} & \sqrt[2]{2}c_{14} & \sqrt[2]{2}c_{15} & \sqrt[2]{2}c_{16} & e_{11} & e_{21} & e_{31} \\ c_{21} & c_{22} & c_{23} & \sqrt[2]{2}c_{24} & \sqrt[2]{2}c_{25} & \sqrt[2]{2}c_{26} & e_{12} & e_{22} & e_{32} \\ c_{31} & c_{32} & c_{33} & \sqrt[2]{2}c_{34} & \sqrt[2]{2}c_{35} & \sqrt[2]{2}c_{36} & e_{13} & e_{23} & e_{33} \\ \sqrt[2]{2}c_{41} & \sqrt[2]{2}c_{42} & \sqrt[2]{2}c_{43} & 2c_{44} & 2c_{45} & 2c_{46} & e_{14} & e_{24} & e_{34} \\ \sqrt[2]{2}c_{51} & \sqrt[2]{2}c_{52} & \sqrt[2]{2}c_{53} & 2c_{54} & 2c_{55} & 2c_{56} & e_{15} & e_{25} & e_{35} \\ \sqrt[2]{2}c_{61} & \sqrt[2]{2}c_{62} & \sqrt[2]{2}c_{63} & 2c_{64} & 2c_{65} & 2c_{66} & e_{16} & e_{26} & e_{36} \\ e_{11} & e_{12} & e_{13} & e_{14} & e_{15} & e_{16} & -\kappa_{11} & -\kappa_{12} & -\kappa_{13} \\ e_{21} & e_{22} & e_{23} & e_{24} & e_{25} & e_{26} & -\kappa_{21} & -\kappa_{22} & -\kappa_{23} \\ e_{31} & e_{32} & e_{33} & e_{34} & e_{35} & e_{36} & -\kappa_{31} & -\kappa_{33} & -\kappa_{33} \end{pmatrix} \tag{2.2}$$

Further simplified as shown by Aguiar, Bravo-Castillero, and Silva [13] presuming isotropy in two directions, but converted to Kelvin-Mandel Notation, the electromechanical coupling moduli $\mathbf{M}$ reads as in Equation 2.3.

$$\mathbf{M} = \begin{pmatrix} c_{11} & c_{12} & c_{13} & 0 & 0 & 0 & 0 & 0 & e_{31} \\ c_{12} & c_{11} & c_{13} & 0 & 0 & 0 & 0 & 0 & e_{31} \\ c_{13} & c_{13} & c_{33} & 0 & 0 & 0 & 0 & 0 & e_{33} \\ 0 & 0 & 0 & 2c_{44} & 0 & 0 & e_{14} & e_{15} & 0 \\ 0 & 0 & 0 & 0 & 2c_{44} & 0 & e_{15} & -e_{14} & 0 \\ 0 & 0 & 0 & 0 & 0 & 2c_{66} & 0 & 0 & 0 \\ 0 & 0 & 0 & e_{14} & e_{15} & 0 & -\kappa_{11} & 0 & 0 \\ 0 & 0 & 0 & e_{15} & -e_{14} & 0 & 0 & -\kappa_{11} & 0 \\ e_{31} & e_{31} & e_{33} & 0 & 0 & 0 & 0 & 0 & -\kappa_{33} \end{pmatrix} \tag{2.3}$$

3 Material homogenization procedure

To handle a composite as a homogeneous material, in spite of its consistency of multiple phases, Zaoui [14, eq. 20], or in a more general format Fritsch and Hellmich [15, eq. 1] stated methods to estimate the elasticity of the homogenized material. However, the homogenization procedure is only valid, if the different size scales are in a specific scope.

When extended to calculate the piezoelectric and dielectric moduli, in addition to the elastic moduli, but simplified to be practicable with Voigt or Kelvin-Mandel notation the equations are stated as followed in Equation 3.1, where $\mathbf{M}_{est}$ are the electromechanical properties of the new estimated material, $\mathbf{M}_0$ represents the electromechanical properties of the primary material, s, r are the different phases and f_s the corresponding volume fractions, $\mathbf{S}_s$ are the Piezo-Eshelby tensor (see chapter 4) and $\mathbf{M}_s$ the electromechanical material parameters for the different phases.

$$\mathbf{M}_{est} = \left(\sum_r f_r \mathbf{M}_r \cdot [\mathbb{I} + \underbrace{\mathbf{S}_r \cdot \mathbf{M}_r^{-1}}_{\mathbf{P}_r} \cdot (\mathbf{M}_r - \mathbf{M}_0)]^{-1} \right) \cdot \left(\sum_s f_s [\mathbb{I} + \underbrace{\mathbf{S}_s \cdot \mathbf{M}_s^{-1}}_{\mathbf{P}_s} \cdot (\mathbf{M}_s - \mathbf{M}_0)]^{-1} \right)^{-1} \tag{3.1}$$

Although there is a general formulation with fourth-order tensors for this [15], a reduction to this equations with second-order tensors, which can be written down as matrices, is needed to compute the parameters. Under certain circumstances there are ways to calculate the inverse of a fourth-order tensor, which is also reversible [16], but not fulfilling the criterion of the identity tensor A_{abcd}: $A^{-1}_{abcd} = \mathbb{I}_{abcd}$.

The calculations in the following chapters are done with the Kelvin-Mandel matrix notation, therefore the elastic shear values need to be corrected after calculating the material properties matrix $\mathbf{M}$.

3.1 Homogenization concept

The concept of this calculation is, that in a representative volume element, multiple different materials with different material properties are contained. While mechanical stress and strain can be averaged along the geometry, leading to a correct result, this is not possible for the stiffness of the material. This means, the macroscopic mechanical strain $\mathcal{E}$, which accounts for the representative volume Element, equals the average of the microscopic mechanical strain $\boldsymbol{\varepsilon}$, which depends on its spatial position. For a linear concentration problem exists a down-scaling tensor $\mathbb{A}_1$ describing the relation of between the macroscopic and microscopic property.

$$\mathcal{E} = \langle \boldsymbol{\varepsilon} \rangle^1 \tag{3.2a}$$

$$\boldsymbol{\varepsilon}(x) = \mathbb{A}_1(x) : \mathcal{E} \tag{3.2b}$$

The relation between the macroscopic fourth-order stiffness tensor $\mathbb{C}$ and the microscopic fourth-order stiffness tensor $\mathbb{c}$, also dependent from its spacial position, reads as:

$$\mathbb{C} = \langle \mathbb{c}(x) : \mathbb{A}_1(x) \rangle \tag{3.3}$$

Simplifying the model from an infinite amount of different micro structures to a handful of phases with defined and homogeneous material properties gives the possibility to write the macroscopic mechanical strain $\mathcal{E}$ as the sum of the strain in the phases $\boldsymbol{\varepsilon}_r$ and the corresponding volume fractions f_r, where r is indicating the different phases.

$$\mathcal{E} = \sum_r f_r \boldsymbol{\varepsilon}_r \tag{3.4a}$$

$$\mathbb{C}^{estimated} = \sum_r f_r \mathbb{c}_r : \mathbb{A}_r^{estimated} \tag{3.4b}$$

With the Hill tensor $\mathbb{P}$, an estimation for the down-scaling tensor $\mathbb{A}_1$ can be made for a homogeneity under the effect of some strain at infinity $\mathcal{E}^\infty$. The stiffness is represented by $\mathbb{c}_r$ for the individual phases and $\mathbb{C}^\infty$ for the infinite matrix where the phases are embedded. The unity tensor $\mathbb{I}$ can be represented as an identity matrix, if this scheme is applied to second-order tensors.

[1] $\langle a \rangle$ is representing the average of a and results from the respective volume integral $\int_V \boldsymbol{\varepsilon} \mathrm{d}V = \mathcal{E}\, V$, which can be proofed with the Gauss theorem

$$[\mathbb{I} + \mathbb{P}_r^{\infty} : (\mathbb{c}_r - \mathbb{C}^{\infty})] : \boldsymbol{\varepsilon}_r = \mathcal{E}^{\infty} \tag{3.5}$$
$$\boldsymbol{\varepsilon}_r = [\mathbb{I} + \mathbb{P}_r^{\infty} : (\mathbb{c}_r - \mathbb{C}^{\infty})]^{-1} : \mathcal{E}^{\infty}$$

$$\text{with } \mathcal{E} = \sum_r f_r \boldsymbol{\varepsilon}_r = \sum_r f_r \, [\mathbb{I} + \mathbb{P}_r^{\infty} : (\mathbb{c}_r - \mathbb{C}^{\infty})]^{-1} : \mathcal{E}^{\infty} \tag{3.6}$$
$$\mathcal{E}^{\infty} = \left[\sum_r f_r \, [\mathbb{I} + \mathbb{P}_r^{\infty} : (\mathbb{c}_r - \mathbb{C}^{\infty})]^{-1} \right]^{-1} : \mathcal{E}$$
$$[\mathbb{I} + \mathbb{P}_r^{\infty} : (\mathbb{c}_r - \mathbb{C}^{\infty})] : \boldsymbol{\varepsilon}_r = \left[\sum_r f_r \, [\mathbb{I} + \mathbb{P}_r^{\infty} : (\mathbb{c}_r - \mathbb{C}^{\infty})]^{-1} \right]^{-1} : \mathcal{E}$$

(3.7)

$$\text{and } \boldsymbol{\varepsilon}(x) = \mathbb{A}_1(x) : \mathcal{E} \tag{3.8}$$
$$\boldsymbol{\varepsilon}_r = [\mathbb{I} + \mathbb{P}_r^{\infty} : (\mathbb{c}_r - \mathbb{C}^{\infty})]^{-1} : \left[\sum_r f_r \, [\mathbb{I} + \mathbb{P}_r^{\infty} : (\mathbb{c}_r - \mathbb{C}^{\infty})]^{-1} \right]^{-1} : \mathcal{E}$$
$$\mathbb{A}_r^{estimated} = [\mathbb{I} + \mathbb{P}_r^{\infty} : (\mathbb{c}_r - \mathbb{C}^{\infty})]^{-1} : \left[\sum_r f_r \, [\mathbb{I} + \mathbb{P}_r^{\infty} : (\mathbb{c}_r - \mathbb{C}^{\infty})]^{-1} \right]^{-1}$$

Using the result from Equation 3.8 and inserting them in Equation 3.4b, the equation as in Equation 3.1 is achieved, but only for the mechanical aspects. According to that, the Hill tensor $\mathbb{P}$ has to correspond only to the mechanical quantities.

$$\mathbb{C}^{estimated} = \left(\sum_r f_r \mathbb{c}_r : [\mathbb{I} + \mathbb{P}_r : (\mathbb{c}_r - \mathbb{C}_0)]^{-1} \right) : \left(\sum_s f_s [\mathbb{I} + \mathbb{P}_s : (\mathbb{c}_s - \mathbb{C}_0)]^{-1} \right)^{-1} \tag{3.9}$$

The electric field $\vec{E}$ and displacement $\vec{D}$ are following a similar concept as the stress-strain relation, with the corresponding material moduli. Extending this system by adding the permittivity and piezoelectric constants, and simplifying from a general fourth-order tensor notation yields Equation 3.1.

$$\vec{\sigma} = \mathbf{c} \cdot \vec{\varepsilon} - \boldsymbol{e}' \cdot \vec{E} \tag{3.10}$$
$$\vec{D} = \boldsymbol{e} \cdot \vec{\varepsilon} + \boldsymbol{\kappa} \cdot \vec{E}$$

$$\text{equals to } \begin{bmatrix} \vec{\sigma} \\ \vec{D} \end{bmatrix} = \mathbf{M} \cdot \begin{bmatrix} \vec{\varepsilon} \\ -\vec{E} \end{bmatrix} \tag{3.11}$$

3.2 Homogenization of dielectric moduli

Analog to the mechanical part, this concept also works with the dielectric moduli. The macroscopic dielectric moduli $\boldsymbol{K}$ and the position-depending microscopic dielectric moduli $\boldsymbol{\kappa}$ are linked with the down-scaling tensor $\boldsymbol{\Gamma}_1$, as in Equation 3.12a. From Equation 3.11, disregarding the mechanical strain, the local displacement $\vec{D}$ is linked with the microscopic electric field $\vec{E}_{mic}$ via the dielectric properties of the material. Hereby may be noted, that the notation changes, since the dielectric moduli are second-order tensors, unlike the fourth-order stiffness tensors.

$$\boldsymbol{K} = \langle \boldsymbol{\kappa}(x) \cdot \boldsymbol{\Gamma}_1(x) \rangle \tag{3.12a}$$

$$\vec{D} = \boldsymbol{\kappa} \cdot \vec{E}_{mic} \tag{3.12b}$$

Like with the mechanical strain, the macroscopic electric field $\vec{E}_{MAC}$ can be obtained by the microscopic electric field $\vec{E}_{mic}$, knowing the spatial dispersion.

$$\vec{E}_{MAC} = \langle \vec{E}_{mic} \rangle \tag{3.13a}$$

$$\vec{E}_{mic}(x) = \boldsymbol{\Gamma}_1(x) \cdot \vec{E}_{MAC} \tag{3.13b}$$

Assuming the inhomogeneities lumped to intrinsic homogeneous phases, allows to describe macroscopic quantities as sums of the microscopic, with the corresponding volume fraction f_s, where s depicts the individual phase.

$$\vec{E}_{MAC} = \sum_r f_r \vec{E}_{mic,r} \tag{3.14a}$$

$$\boldsymbol{K}^{estimated} = \sum_r f_r \boldsymbol{\kappa}_r \cdot \boldsymbol{\Gamma}_r^{estimated} \tag{3.14b}$$

Introducing an assumption for the behavior of the phases, an estimated down-scaling tensor can be obtained. This assumption requires a 3×3 Hill tensor, respecting the interactions of dielectric properties.

$$\begin{aligned} [\mathbb{I} + \mathbf{P}_r^{\infty} \cdot (\boldsymbol{\kappa}_r - \boldsymbol{K}^{\infty})] \cdot \vec{E}_{mic,r} &= \vec{E}_{MAC}^{\infty} \\ \vec{E}_{mic,r} &= [\mathbb{I} + \mathbf{P}_r^{\infty} \cdot (\boldsymbol{\kappa}_r - \boldsymbol{K}^{\infty})]^{-1} \cdot \vec{E}_{MAC}^{\infty} \end{aligned} \tag{3.15}$$

$$\text{with } \vec{E}_{MAC} = \sum_r f_r \vec{E}_{mic,r} = \sum_r f_r \left[\mathbb{I} + \mathbf{P}_r^{\infty} \cdot (\boldsymbol{\kappa}_r - \boldsymbol{K}^{\infty})\right]^{-1} \cdot \vec{E}_{MAC}^{\infty} \tag{3.16}$$

$$\vec{E}_{MAC}^{\infty} = \left[\sum_r f_r \left[\mathbb{I} + \mathbf{P}_r^{\infty} \cdot (\boldsymbol{\kappa}_r - \boldsymbol{K}^{\infty})\right]^{-1}\right]^{-1} \cdot \vec{E}_{MAC}$$

$$\left[\mathbb{I} + \mathbf{P}_r^{\infty} \cdot (\boldsymbol{\kappa}_r - \boldsymbol{K}^{\infty})\right] \cdot \vec{E}_{mic,r} = \left[\sum_r f_r \left[\mathbb{I} + \mathbf{P}_r^{\infty} \cdot (\boldsymbol{\kappa}_r - \boldsymbol{K}^{\infty})\right]^{-1}\right]^{-1} \cdot \vec{E}_{MAC}$$

$$\text{and } \vec{E}_{mic}(x) = \boldsymbol{\Gamma}_1(x) \cdot \vec{E}_{MAC} \tag{3.17}$$

$$\vec{E}_{mic,r} = \left[\mathbb{I} + \mathbf{P}_r^{\infty} \cdot (\boldsymbol{\kappa}_r - \boldsymbol{K}^{\infty})\right]^{-1} \cdot \left[\sum_r f_r \left[\mathbb{I} + \mathbf{P}_r^{\infty} \cdot (\boldsymbol{\kappa}_r - \boldsymbol{K}^{\infty})\right]^{-1}\right]^{-1} \cdot \vec{E}_{MAC}$$

$$\boldsymbol{\Gamma}_r^{estimated} = \left[\mathbb{I} + \mathbf{P}_r^{\infty} \cdot (\boldsymbol{\kappa}_r - \boldsymbol{K}^{\infty})\right]^{-1} \cdot \left[\sum_r f_r \left[\mathbb{I} + \mathbf{P}_r^{\infty} \cdot (\boldsymbol{\kappa}_r - \boldsymbol{K}^{\infty})\right]^{-1}\right]^{-1}$$

This leads to the homogenized dielectric properties, strongly resembling the scheme in Equation 3.9, where $\boldsymbol{K}_0$ is the tensor of the dielectric properties from the matrix material.

$$\boldsymbol{K}^{estimated} = \left(\sum_r f_r \boldsymbol{\kappa}_r \cdot \left[\mathbb{I} + \mathbf{P}_r \cdot (\boldsymbol{\kappa}_r - \boldsymbol{K}_0)\right]^{-1}\right) \cdot \left(\sum_s f_s \left[\mathbb{I} + \mathbf{P}_s \cdot (\boldsymbol{\kappa}_s - \boldsymbol{K}_0)\right]^{-1}\right)^{-1} \tag{3.18}$$

3.3 Homogenization of piezoelectric moduli

Since the electric field perpendicular to a plane can be averaged along this plane and yields a macroscopic value, affecting this respective plane, the same concept can be used for the mechanical strain. Because the behavior between the macroscopic and microscopic scopes of this physical quantities is the same, the following equations will strongly resemble these from section 3.1.

As mentioned just now, the macroscopic electric field $\vec{E}_{MAC}$ is the average of the microscopic electric field $\vec{E}_{mic}$ and their relation can be described by a down-scaling tensor $\boldsymbol{B}_1$.

$$\vec{E}_{MAC} = \langle \vec{E}_{mic} \rangle \tag{3.19a}$$

$$\vec{E}_{mic}(x) = \boldsymbol{B}_1(x) \cdot \vec{E}_{MAC} \tag{3.19b}$$

The relation between the macroscopic piezo tensor $\boldsymbol{e}_{MAC}$ and the microscopic piezo tensor $\boldsymbol{e}_{mic}$ can not be described by simple averaging, but resembles the average in respect to the spacial distribution, described by the down-scaling tensor $\boldsymbol{B}_1$.

$$\boldsymbol{e'}_{MAC} = \langle \boldsymbol{e'}_{mic}(x) \cdot \boldsymbol{B}_1(x) \rangle \tag{3.20a}$$

$$\sigma = -\boldsymbol{e'}_{mic} \cdot \vec{E}_{mic} \tag{3.20b}$$

Again by reducing the complexity of all micro structures to a finite amount of material phases, the relation of macroscopic and microscopic quantities can be written as a sum. Each phase has homogeneous piezo properties $\boldsymbol{e}_r$ and a corresponding volume fraction f_r, where r indicates the individual phases.

$$\vec{E}_{MAC} = \sum_r f_r \vec{E}_{mic,r} \tag{3.21a}$$

$$\boldsymbol{e'}^{estimated}_{MAC} = \sum_r f_r \boldsymbol{e'}_r \cdot \boldsymbol{B}^{estimated}_r \tag{3.21b}$$

To find an assumption for the down-scaling tensor $\boldsymbol{B}_1$, the Hill tensor P is used, but in this case the Hill tensor covers only the piezoelectric properties of the material.

$$\begin{aligned} \left[\mathbb{I} + \mathbf{P}^{\infty}_r \cdot (\boldsymbol{e'}_r - \boldsymbol{e'}^{\infty}_{MAC})\right] \cdot \vec{E}_{mic,r} &= \vec{E}^{\infty}_{MAC} \\ \vec{E}_{mic,r} &= \left[\mathbb{I} + \mathbf{P}^{\infty}_r \cdot (\boldsymbol{e'}_r - \boldsymbol{e'}^{\infty}_{MAC})\right]^{-1} \cdot \vec{E}^{\infty}_{MAC} \end{aligned} \tag{3.22}$$

$$\text{with } \vec{E}_{MAC} = \sum_r f_r \vec{E}_{mic,r} = \sum_r f_r \left[\mathbb{I} + \mathbf{P}_r^{\infty} \cdot (\boldsymbol{e}'_r - \boldsymbol{e}'^{\infty}_{MAC})\right]^{-1} \cdot \vec{E}^{\infty}_{MAC} \quad (3.23)$$

$$\vec{E}^{\infty}_{MAC} = \left[\sum_r f_r \left[\mathbb{I} + \mathbf{P}_r^{\infty} \cdot (\boldsymbol{e}'_r - \boldsymbol{e}'^{\infty}_{MAC})\right]^{-1}\right]^{-1} \cdot \vec{E}_{MAC}$$

$$\left[\mathbb{I} + \mathbf{P}_r^{\infty} \cdot (\boldsymbol{e}'_r - \boldsymbol{e}'^{\infty}_{MAC})\right] \cdot \vec{E}_{mic,r} = \left[\sum_r f_r \left[\mathbb{I} + \mathbf{P}_r^{\infty} \cdot (\boldsymbol{e}'_r - \boldsymbol{e}'^{\infty}_{MAC})\right]^{-1}\right]^{-1} \cdot \vec{E}_{MAC}$$

$$\text{and } \vec{E}_{mic}(x) = \boldsymbol{B}_1(x) \cdot \vec{E}_{MAC} \quad (3.24)$$

$$\vec{E}_{mic,r} = \left[\mathbb{I} + \mathbf{P}_r^{\infty} \cdot (\boldsymbol{e}'_r - \boldsymbol{e}'^{\infty}_{MAC})\right]^{-1} \cdot \left[\sum_r f_r \left[\mathbb{I} + \mathbf{P}_r^{\infty} \cdot (\boldsymbol{e}'_r - \boldsymbol{e}'^{\infty}_{MAC})\right]^{-1}\right]^{-1} \cdot \vec{E}_{MAC}$$

$$\boldsymbol{B}_r^{estimated} = \left[\mathbb{I} + \mathbf{P}_r^{\infty} \cdot (\boldsymbol{e}'_r - \boldsymbol{e}'^{\infty}_{MAC})\right]^{-1} \cdot \left[\sum_r f_r \left[\mathbb{I} + \mathbf{P}_r^{\infty} \cdot (\boldsymbol{e}'_r - \boldsymbol{e}'^{\infty}_{MAC})\right]^{-1}\right]^{-1}$$

This evaluation leads to similar results like with the elastic moduli, but with the unfavorable property of the piezoelectric moduli. Because the piezoelectric moduli e are represented as a 3×6 matrix, this calculation requires a Moore-Penrose inverse, not ensuring correct simulation results. Adding the mechanical and electrical component to one calculation bypasses this problem, since it results in a 9×9 matrix, which can be inverted regularly.

3.4 Combined homogenization method

At this step, the individual homogenization methods should be combined to a single one. To find an algorithm to calculate the combined material profile, the averaging concept of all material moduli have to be considered.

$$\mathbb{C} = \langle \mathbb{c}(x) : \mathbb{A}_1(x) \rangle \tag{3.25a}$$
$$\boldsymbol{e'}_{MAC} = \langle \boldsymbol{e'}_{mic}(x) \cdot \boldsymbol{B}_1(x) \rangle \tag{3.25b}$$
$$\boldsymbol{e}_{MAC} = \langle \boldsymbol{e}_{mic}(x) \cdot \boldsymbol{B}_2(x) \rangle \tag{3.25c}$$
$$\boldsymbol{K} = \langle \boldsymbol{\kappa}(x) \cdot \boldsymbol{\Gamma}_1(x) \rangle \tag{3.25d}$$

To combine the material properties, all moduli have to be reduced to second-order tensors, using material symmetries. This makes it possible to write down all moduli in a 9×9 matrix. Also the double contractions for the fourth-order elasticity moduli are simplified to dot products.

Getting out the microscopic moduli from the averaging concept to an individual matrix, requires the introduction of new down-scaling tensors $\tilde{\boldsymbol{A}}_1, \tilde{\boldsymbol{B}}_1, \tilde{\boldsymbol{B}}_2, \tilde{\boldsymbol{\Gamma}}_1$, which respect the influence of multiple input quantities on their material parameter, but are unknown at this point. The new down-scaling tensors can be combined to one matrix $\tilde{\boldsymbol{N}}$.

$$\begin{aligned}
\begin{pmatrix} \mathbf{C} & \boldsymbol{e'}_{MAC} \\ \boldsymbol{e}_{MAC} & -\boldsymbol{K} \end{pmatrix} &= \begin{pmatrix} \langle \mathbf{c}(x) \cdot \boldsymbol{A}_1(x) \rangle & \langle \boldsymbol{e'}_{mic}(x) \cdot \boldsymbol{B}_1(x) \rangle \\ \langle \boldsymbol{e}_{mic}(x) \cdot \boldsymbol{B}_2(x) \rangle & \langle -\boldsymbol{\kappa}(x) \cdot \boldsymbol{\Gamma}_1(x) \rangle \end{pmatrix} \\
&= \left\langle \begin{pmatrix} \mathbf{c}(x) & \boldsymbol{e'}_{mic}(x) \\ \boldsymbol{e}_{mic}(x) & -\boldsymbol{\kappa}(x) \end{pmatrix} \cdot \underbrace{\begin{pmatrix} \tilde{\boldsymbol{A}}_1(x) & \tilde{\boldsymbol{B}}_1(x) \\ \tilde{\boldsymbol{B}}_2(x) & \tilde{\boldsymbol{\Gamma}}_1(x) \end{pmatrix}}_{\tilde{\boldsymbol{N}}(x)} \right\rangle \\
&= \left\langle \begin{pmatrix} \mathbf{c}(x) & \boldsymbol{e'}_{mic}(x) \\ \boldsymbol{e}_{mic}(x) & -\boldsymbol{\kappa}(x) \end{pmatrix} \cdot \tilde{\boldsymbol{N}}(x) \right\rangle
\end{aligned} \tag{3.26}$$

As already shown in Equation 3.11, the input quantities can be added together to a vector of rank 9. Further the simplification to a finite amount of homogeneous

material phases also applies to the combined material matrix and the corresponding input quantities, which are mechanical strain and electric field strength.

$$\begin{pmatrix} \vec{\mathcal{E}} \\ -\vec{E}_{MAC} \end{pmatrix} = \sum_r f_r \begin{pmatrix} \vec{\varepsilon}_r \\ -\vec{E}_{mic} \end{pmatrix} \tag{3.27a}$$

$$\begin{pmatrix} \mathbf{C} & \boldsymbol{e}'_{MAC} \\ \boldsymbol{e}_{MAC} & -\boldsymbol{K} \end{pmatrix}^{estimated} = \sum_r f_r \begin{pmatrix} \mathbf{c}_r & \boldsymbol{e}'_r \\ \boldsymbol{e}_r & -\boldsymbol{\kappa}_r \end{pmatrix} \cdot \tilde{\boldsymbol{N}}_r^{estimated} \tag{3.27b}$$

With a matching Hill tensor to describe the impact of inhomogeneity in a matrix and some mathematical transformations, it is possible to obtain an estimation for the down-scaling matrix $\tilde{\boldsymbol{N}}$. This of course requires a Hill tensor that considers the interaction of all material parameters. The concept of creating a matching Hill tensor is more precisely stated in chapter 4.

$$\left[\mathbb{I} + \mathbf{P}_r^{\infty} \cdot \left(\begin{pmatrix} \mathbf{c}_r & \boldsymbol{e}'_r \\ \boldsymbol{e}_r & -\boldsymbol{\kappa}_r \end{pmatrix} - \begin{pmatrix} \mathbf{C}^{\infty} & \boldsymbol{e}'^{\infty}_{MAC} \\ \boldsymbol{e}^{\infty}_{MAC} & \boldsymbol{K}^{\infty} \end{pmatrix} \right) \right] \cdot \begin{pmatrix} \vec{\varepsilon}_r \\ -\vec{E}_{mic} \end{pmatrix} = \begin{pmatrix} \vec{\mathcal{E}}^{\infty} \\ -\vec{E}^{\infty}_{MAC} \end{pmatrix} \tag{3.28}$$

$$\begin{pmatrix} \vec{\varepsilon}_r \\ -\vec{E}_{mic} \end{pmatrix} = \left[\mathbb{I} + \mathbf{P}_r^{\infty} \cdot \left(\begin{pmatrix} \mathbf{c}_r & \boldsymbol{e}'_r \\ \boldsymbol{e}_r & -\boldsymbol{\kappa}_r \end{pmatrix} - \begin{pmatrix} \mathbf{C}^{\infty} & e'^{\infty}_{MAC} \\ \boldsymbol{e}^{\infty}_{MAC} & \boldsymbol{K}^{\infty} \end{pmatrix} \right) \right]^{-1} \cdot \begin{pmatrix} \vec{\mathcal{E}}^{\infty} \\ -\vec{E}^{\infty}_{MAC} \end{pmatrix}$$

$$\text{with } \begin{pmatrix} \vec{\mathcal{E}} \\ -\vec{E}_{MAC} \end{pmatrix} = \sum_r f_r \begin{pmatrix} \vec{\varepsilon}_r \\ -\vec{E}_{mic} \end{pmatrix} \tag{3.29}$$

$$= \sum_r f_r \left[\mathbb{I} + \mathbf{P}_r^{\infty} \cdot \left(\begin{pmatrix} \mathbf{c}_r & \boldsymbol{e}'_r \\ \boldsymbol{e}_r & -\boldsymbol{\kappa}_r \end{pmatrix} - \begin{pmatrix} \mathbf{C}^{\infty} & \boldsymbol{e}'^{\infty}_{MAC} \\ \boldsymbol{e}^{\infty}_{MAC} & \boldsymbol{K}^{\infty} \end{pmatrix} \right) \right]^{-1} \cdot \begin{pmatrix} \vec{\mathcal{E}}^{\infty} \\ -\vec{E}^{\infty}_{MAC} \end{pmatrix}$$

$$\begin{pmatrix} \vec{\mathcal{E}}^{\infty} \\ -\vec{E}^{\infty}_{MAC} \end{pmatrix} = \left[\sum_r f_r \left[\mathbb{I} + \mathbf{P}_r^{\infty} \cdot \left(\begin{pmatrix} \mathbf{c}_r & \boldsymbol{e}'_r \\ \boldsymbol{e}_r & -\boldsymbol{\kappa}_r \end{pmatrix} - \begin{pmatrix} \mathbf{C}^{\infty} & \boldsymbol{e}'^{\infty}_{MAC} \\ \boldsymbol{e}^{\infty}_{MAC} & \boldsymbol{K}^{\infty} \end{pmatrix} \right) \right]^{-1} \right]^{-1} \cdot \begin{pmatrix} \vec{\mathcal{E}} \\ -\vec{E}_{MAC} \end{pmatrix}$$

$$\left[\mathbb{I} + \mathbf{P}_r^{\infty} \cdot \left(\begin{pmatrix} \mathbf{c}_r & \boldsymbol{e}'_r \\ \boldsymbol{e}_r & -\boldsymbol{\kappa}_r \end{pmatrix} - \begin{pmatrix} \mathbf{C}^{\infty} & \boldsymbol{e}'^{\infty}_{MAC} \\ \boldsymbol{e}^{\infty}_{MAC} & \boldsymbol{K}^{\infty} \end{pmatrix} \right) \right] \cdot \begin{pmatrix} \vec{\varepsilon}_r \\ -\vec{E}_{mic} \end{pmatrix} = \tag{3.30}$$

$$\left[\sum_r f_r \left[\mathbb{I} + \mathbf{P}_r^{\infty} \cdot \left(\begin{pmatrix} \mathbf{c}_r & \boldsymbol{e}'_r \\ \boldsymbol{e}_r & -\boldsymbol{\kappa}_r \end{pmatrix} - \begin{pmatrix} \mathbf{C}^{\infty} & \boldsymbol{e}'^{\infty}_{MAC} \\ \boldsymbol{e}^{\infty}_{MAC} & \boldsymbol{K}^{\infty} \end{pmatrix} \right) \right]^{-1} \right]^{-1} \cdot \begin{pmatrix} \vec{\mathcal{E}} \\ -\vec{E}_{MAC} \end{pmatrix}$$

$$\text{and} \quad \begin{pmatrix} \vec{\varepsilon}(x) \\ -\vec{E}_{mic}(x) \end{pmatrix} = \tilde{\boldsymbol{N}}(x) \cdot \begin{pmatrix} \vec{\mathcal{E}} \\ -\vec{E}_{MAC} \end{pmatrix} \tag{3.31}$$

$$\begin{aligned} \begin{pmatrix} \vec{\varepsilon}_r \\ -\vec{E}_{mic} \end{pmatrix} = &\left[\mathbb{I} + \mathbf{P}_r^{\infty} \cdot \left(\begin{pmatrix} \mathbf{c}_r & \boldsymbol{e}'_r \\ \boldsymbol{e}_r & -\boldsymbol{\kappa}_r \end{pmatrix} - \begin{pmatrix} \mathbf{C}^{\infty} & \boldsymbol{e}'^{\infty}_{MAC} \\ \boldsymbol{e}^{\infty}_{MAC} & \boldsymbol{K}^{\infty} \end{pmatrix} \right) \right]^{-1} \\ &\cdot \left[\sum_r f_r \left[\mathbb{I} + \mathbf{P}_r^{\infty} \cdot \left(\begin{pmatrix} \mathbf{c}_r & \boldsymbol{e}'_r \\ \boldsymbol{e}_r & -\boldsymbol{\kappa}_r \end{pmatrix} - \begin{pmatrix} \mathbf{C}^{\infty} & \boldsymbol{e}'^{\infty}_{MAC} \\ \boldsymbol{e}^{\infty}_{MAC} & \boldsymbol{K}^{\infty} \end{pmatrix} \right) \right]^{-1} \right]^{-1} \cdot \begin{pmatrix} \vec{\mathcal{E}} \\ -\vec{E}_{MAC} \end{pmatrix} \end{aligned} \tag{3.32}$$

$$\begin{aligned} \tilde{\boldsymbol{N}}_r^{estimated} = &\left[\mathbb{I} + \mathbf{P}_r^{\infty} \cdot \left(\begin{pmatrix} \mathbf{c}_r & \boldsymbol{e}'_r \\ \boldsymbol{e}_r & -\boldsymbol{\kappa}_r \end{pmatrix} - \begin{pmatrix} \mathbf{C}^{\infty} & \boldsymbol{e}'^{\infty}_{MAC} \\ \boldsymbol{e}^{\infty}_{MAC} & \boldsymbol{K}^{\infty} \end{pmatrix} \right) \right]^{-1} \\ &\cdot \left[\sum_r f_r \left[\mathbb{I} + \mathbf{P}_r^{\infty} \cdot \left(\begin{pmatrix} \mathbf{c}_r & \boldsymbol{e}'_r \\ \boldsymbol{e}_r & -\boldsymbol{\kappa}_r \end{pmatrix} - \begin{pmatrix} \mathbf{C}^{\infty} & \boldsymbol{e}'^{\infty}_{MAC} \\ \boldsymbol{e}^{\infty}_{MAC} & \boldsymbol{K}^{\infty} \end{pmatrix} \right) \right]^{-1} \right]^{-1} \end{aligned} \tag{3.33}$$

Filling in the estimation of $\tilde{\boldsymbol{N}}$ for all present phases, as in Equation 3.27b, an expression for a homogenized material can be obtained, as in Equation 3.34. Contracting all material moduli to the matrix $\mathbf{M}$ yields the same homogenization formula as in Equation 3.1.

$$\text{with} \quad \begin{pmatrix} \mathbf{C} & \boldsymbol{e}'_{MAC} \\ \boldsymbol{e}_{MAC} & -\boldsymbol{K} \end{pmatrix}^{estimated} = \sum_r f_r \begin{pmatrix} \mathbf{c}_r & \boldsymbol{e}'_r \\ \boldsymbol{e}_r & -\boldsymbol{\kappa}_r \end{pmatrix} \cdot \tilde{\boldsymbol{N}}_r^{estimated}$$

$$\begin{aligned} \overbrace{\begin{pmatrix} \mathbf{C} & \boldsymbol{e}'_{MAC} \\ \boldsymbol{e}_{MAC} & -\boldsymbol{K} \end{pmatrix}^{estimated}}^{\mathbf{M}_{est}} = &\left(\sum_r f_r \overbrace{\begin{pmatrix} \mathbf{c}_r & \boldsymbol{e}'_r \\ \boldsymbol{e}_r & -\boldsymbol{\kappa}_r \end{pmatrix}}^{\mathbf{M}_r} \cdot \left[\mathbb{I} + \mathbf{P}_r \cdot \left(\overbrace{\begin{pmatrix} \mathbf{c}_r & \boldsymbol{e}'_r \\ \boldsymbol{e}_r & -\boldsymbol{\kappa}_r \end{pmatrix}}^{\mathbf{M}_r} - \overbrace{\begin{pmatrix} \mathbf{C}^{\infty} & \boldsymbol{e}'^{\infty}_{MAC} \\ \boldsymbol{e}^{\infty}_{MAC} & \boldsymbol{K}^{\infty} \end{pmatrix}}^{\mathbf{M}_0} \right) \right]^{-1} \right) \\ &\cdot \left(\sum_s f_s \left[\mathbb{I} + \mathbf{P}_s \cdot \left(\underbrace{\begin{pmatrix} \mathbf{c}_r & \boldsymbol{e}'_r \\ \boldsymbol{e}_r & -\boldsymbol{\kappa}_r \end{pmatrix}}_{\mathbf{M}_s} - \underbrace{\begin{pmatrix} \mathbf{C}^{\infty} & \boldsymbol{e}'^{\infty}_{MAC} \\ \boldsymbol{e}^{\infty}_{MAC} & \boldsymbol{K}^{\infty} \end{pmatrix}}_{\mathbf{M}_0} \right) \right]^{-1} \right)^{-1} \end{aligned} \tag{3.34}$$

4 Piezo-Eshelby Tensor

The Piezo-Eshelby tensor is a fourth-order tensor describing the impact of the exact geometry of the included ellipsoidal.

4.1 Voigt notation

To handle the material parameters $\mathbf{M}$ in Voigt notation, it is necessary to use this concept for the Piezo-Eshelby- and Piezo-Hill tensor as well, which reads as in Equation 4.1.

$$\boldsymbol{M}_{AbCd} = \begin{pmatrix} M_{1111} & M_{1122} & M_{1133} & M_{1132} & M_{1131} & M_{1121} & M_{1141} & M_{1142} & M_{1143} \\ M_{2211} & M_{2222} & M_{2233} & M_{2232} & M_{2231} & M_{2221} & M_{2241} & M_{2242} & M_{2243} \\ M_{3311} & M_{3322} & M_{3333} & M_{3332} & M_{3331} & M_{3321} & M_{3341} & M_{3342} & M_{3343} \\ M_{3211} & M_{3222} & M_{3233} & M_{3232} & M_{3231} & M_{3221} & M_{3241} & M_{3242} & M_{3243} \\ M_{3111} & M_{3122} & M_{3133} & M_{3132} & M_{3131} & M_{3121} & M_{3141} & M_{3142} & M_{3143} \\ M_{2111} & M_{2122} & M_{2133} & M_{2132} & M_{2131} & M_{2121} & M_{2141} & M_{2142} & M_{2143} \\ M_{4111} & M_{4122} & M_{4133} & M_{4132} & M_{4131} & M_{4121} & M_{4141} & M_{4142} & M_{4143} \\ M_{4211} & M_{4222} & M_{4233} & M_{4232} & M_{4231} & M_{4221} & M_{4241} & M_{4242} & M_{4243} \\ M_{4311} & M_{4322} & M_{4333} & M_{4332} & M_{4331} & M_{4321} & M_{4341} & M_{4142} & M_{4343} \end{pmatrix} \tag{4.1}$$

For $A, C \in \mathbb{N}[1...4]$ and $b, d \in \mathbb{N}[1...3]$.

This notation is valid, as long as the symmetry condition for the tensor is respected, as $\boldsymbol{M}_{1212} = \boldsymbol{M}_{2121} = \boldsymbol{M}_{1221} = \boldsymbol{M}_{2112}$

4.2 Calculation of a Piezo-Eshelby Tensor

Mikata stated in his papers [17], [18] how to calculate a Piezo-Eshelby tensor for cylindrical and spherical inclusions, but he assumed that the piezo modulus e_{14} is zero. For the bone building materials e_{14} is an important modulus, therefore the following notation is the same as in the stated papers, but with the value e_{14} added.

The following equations show the general path to constructing a Piezo-Eshelby Tensor. Notice that a fourth-order representation of the material Tensor $\mathbb{M}$ is used. The variable $\vec{y}$ represents the geometric extension, which needs to be parameterized according to the inclusion geometry.

$$\mathbb{S}_{MnAb} = \begin{cases} \frac{1}{8\pi}\mathbb{M}_{iJAb}(I_{inmJ} + I_{imnJ}) & : M \in \{1,2,3\} \\ \frac{1}{4\pi}\mathbb{M}_{iJAb}I_{inAb} & : M = 4 \end{cases} \tag{4.2}$$

$$\boldsymbol{K}_{MJ}(\vec{x}) = \mathbb{M}_{pMJq} \cdot x_i \cdot x_j, \text{ with } \begin{matrix} p,q \in \{1,2,3\} \\ M,J \in \{1,2,3,4\} \end{matrix} \tag{4.3}$$

$$I_{abcd} = \int_{|y|=1} y_a y_b \boldsymbol{K}^{-1}_{cd}(y_1,y_2,y_3)d\vec{y} \tag{4.4}$$

$$\text{with } \vec{y} = y_i \ : \ i \in \{1,2,3\}$$

The matrix K_{MJ} is affected by e_{14} in the following entries and results in total as shown in Equation 4.6.

$$\begin{aligned} K_{24}|_{e_{14}} &= e_{14}x_1x_3 \\ K_{42}|_{e_{14}} &= e_{14}x_1x_3 = K_{24}|_{e_{14}} \\ K_{14}|_{e_{14}} &= -e_{14}x_2x_3 \\ K_{41}|_{e_{14}} &= -e_{14}x_2x_3 = K_{14}|_{e_{14}} \\ K_{34}|_{e_{14}} &= e_{14}x_1x_2 - e_{14}x_1x_2 = 0 \\ K_{43}|_{e_{14}} &= e_{14}x_1x_2 - e_{14}x_1x_2 = 0 \end{aligned} \tag{4.5}$$

$$\boldsymbol{K}_{MJ}(\vec{x}) = \begin{pmatrix} c_{11}\,{x_1}^2 + \left(\frac{c_{11}}{2} - \frac{c_{12}}{2}\right){x_2}^2 + c_{44}\,{x_3}^2 & \frac{x_1\,x_2\,(c_{11}+c_{12})}{2} & x_1\,x_3\,(c_{13}+c_{44}) & x_1\,x_3\,(e_{15}+e_{31}) - e_{14}\,x_2\,x_3 \\ \frac{x_1\,x_2\,(c_{11}+c_{12})}{2} & \left(\frac{c_{11}}{2} - \frac{c_{12}}{2}\right){x_1}^2 + c_{11}\,{x_2}^2 + c_{44}\,{x_3}^2 & x_2\,x_3\,(c_{13}+c_{44}) & x_2\,x_3\,(e_{15}+e_{31}) + e_{14}\,x_1\,x_3 \\ x_1\,x_3\,(c_{13}+c_{44}) & x_2\,x_3\,(c_{13}+c_{44}) & c_{44}\,{x_1}^2 + c_{44}\,{x_2}^2 + c_{33}\,{x_3}^2 & e_{15}\,{x_1}^2 + e_{15}\,{x_2}^2 + e_{33}\,{x_3}^2 \\ x_1\,x_3\,(e_{15}+e_{31}) - e_{14}\,x_2\,x_3 & x_2\,x_3\,(e_{15}+e_{31}) + e_{14}\,x_1\,x_3 & e_{15}\,{x_1}^2 + e_{15}\,{x_2}^2 + e_{33}\,{x_3}^2 & -k_{11}\,{x_1}^2 - k_{11}\,{x_2}^2 - k_{33}\,{x_3}^2 \end{pmatrix} \tag{4.6}$$

4.3 Piezo-Hill tensor

The by Hellmich, Barthélémy, and Dormieux introduced tensor $\mathbb{P}$ [19, eq. 53], called Hill-tensor [15], is only an auxiliary step to compute the following material properties, but has one significant property. This tensor has to be symmetric, when written

as matrix, to produce a symmetric material property matrix $\mathbf{M}$ as in Equation 2.3. In matrix representation, the Hill-tensor $\mathbf{P}$ can be calculated as in Equation 4.7.

$$\mathbf{P} = \mathbf{S} \cdot \mathbf{M}^{-1} \tag{4.7}$$

4.4 Tensor for cylindrical inclusions

Wet collagen appears in the fibril network in a cylindrical shape amongst other structures in bone material [15]. For the following calculations a tensor was used, stated by Mikata, which reads in the matrix notation as Equation 4.10 [17]. The aspect ratio α is the relation of the transversal axes of the elliptic cylinder, characterizing a circle for $\alpha = 1$. The aspect ratio β in the x_3 direction converges to zero, to represent a deformation from a sphere to a cylinder, see chapter 8 to read more about these geometrical factors.

$$\begin{aligned} y_1 &= \sin(\theta)\cos(\phi) & & \\ y_2 &= \alpha \sin(\theta)\sin(\phi) & \phi &\in \mathbb{R}[0, 2\pi) \\ y_3 &= \beta \cos(\theta) & \theta &\in \mathbb{R}[0, \pi) \\ \mathrm{d}\vec{y} &= \sin(\theta)\,\mathrm{d}\theta\,\mathrm{d}\phi & & \end{aligned} \tag{4.8}$$

through $\beta \to 0$ results in:

$$I_{abcd} = \int_{\phi=0}^{2\pi}\int_{\theta=0}^{\pi} y_a y_b K^{-1}_{cd}(y_1, y_2, 0)\sin(\theta)\,\mathrm{d}\theta\,\mathrm{d}\phi \quad \text{with} \begin{matrix} a, b \in \{1, 2\} \\ c, d \in \{1, 2, 3, 4\} \end{matrix} \tag{4.9}$$

Because this Piezo-Eshelby tensor is used for material parameters in Kelvin-Mandel notation, a correction factor of 2 in the entries $S_{cyl4,4}$, $S_{cyl5,5}$ and $S_{cyl6,6}$ distinguishes this tensor from the representation of Mikata [17]. Interestingly all entries of e_{14} and e_{15} fall out, due to the geometry [17, eq. 69]. To evaluate the tensor, the material parameters are not used in SI notation, but with unit prefixes $[c]$ =GPa and $[\kappa]$ =pF/m.

$$\mathbf{S}_{cyl} = \begin{pmatrix} \frac{\alpha}{2(1+\alpha)^2}\left(\frac{3c_{11}+c_{12}}{c_{11}}+\frac{2}{\alpha}\right) & \frac{\alpha}{2(1+\alpha)^2}\left(\frac{(2+\alpha)c_{12}}{\alpha c_{11}}-1\right) & \frac{c_{13}}{(1+\alpha)c_{11}} & 0 & 0 & 0 & 0 & 0 & \frac{e_{31}}{(1+\alpha)c_{11}} \\ \frac{\alpha}{2(1+\alpha)^2}\left(\frac{(1+2\alpha)c_{12}}{c_{11}}-1\right) & \frac{\alpha}{2(1+\alpha)^2}\left(\frac{3c_{11}+c_{12}}{c_{11}}+2\alpha\right) & \frac{\alpha c_{13}}{(1+\alpha)c_{11}} & 0 & 0 & 0 & 0 & 0 & \frac{\alpha e_{31}}{(1+\alpha)c_{11}} \\ 0 & 0 & 0 & 0 & 0 & 0 & 0 & 0 & 0 \\ 0 & 0 & 0 & \frac{\alpha}{2(1+\alpha)} & 0 & 0 & 0 & 0 & 0 \\ 0 & 0 & 0 & 0 & \frac{\alpha}{2(1+\alpha)} & 0 & 0 & 0 & 0 \\ 0 & 0 & 0 & 0 & 0 & \frac{\alpha}{2(1+\alpha)^2}\left(\frac{1+\alpha+\alpha^2}{\alpha}-\frac{c_{12}}{c_{11}}\right) & 0 & 0 & 0 \\ 0 & 0 & 0 & 0 & 0 & 0 & \frac{1}{1+\alpha} & 0 & 0 \\ 0 & 0 & 0 & 0 & 0 & 0 & 0 & \frac{1}{1+\alpha} & 0 \\ 0 & 0 & 0 & 0 & 0 & 0 & 0 & 0 & 0 \end{pmatrix} \tag{4.10}$$

4.5 Tensor for spherical inclusions

The values for I_{abcd} for a spherical inclusion can be obtained by parameterizing the y as the following:

$$\begin{aligned} y_1 &= \sin(\theta)\cos(\phi) & & \\ y_2 &= \alpha\sin(\theta)\sin(\phi) & \phi &\in \mathbb{R}[0, 2\pi) \\ y_3 &= \beta\cos(\theta) & \theta &\in \mathbb{R}[0, \pi) \\ \mathrm{d}\vec{y} &= \sin(\theta)\,\mathrm{d}\theta\,\mathrm{d}\phi & & \end{aligned} \tag{4.11}$$

$$I_{abcd} = \int_{\phi=0}^{2\pi}\int_{\theta=0}^{\pi} y_a y_b K_{cd}^{-1}(y_1, y_2, y_3)\sin(\theta)\,\mathrm{d}\theta\,\mathrm{d}\phi \quad \text{with} \begin{matrix} a, b \in \{1, 2, 3\} \\ c, d \in \{1, 2, 3, 4\} \end{matrix} \tag{4.12}$$

The following work assumes $\alpha = 1$ for spherical inclusions, to keep the calculations in a reasonable scope of complexity. Some of the values of I_{abcd} are zero and have no effect on the Eshelby tensor. Considering the non-zero values, e_{14} has effect on the following values, which need to be calculated to generate the symmetric, second-order Hill tensor $\mathbf{P}$. The following equations are obtained by using Equation 4.2 and Equation 4.7.

$$\begin{aligned} S_{sph,74} &= \frac{1}{4\pi}\left(c_{44}I_{1342} + e_{14}I_{1144}\right) \\ S_{sph,85} &= \frac{1}{4\pi}\left(c_{44}I_{2342} - e_{14}I_{2244}\right) = S_{sph,74} \\ &\text{due to the symmetry } \begin{matrix} I_{1342} = -I_{2342} \\ I_{1144} = I_{2244} \end{matrix} \end{aligned} \tag{4.13}$$

$$\begin{aligned} P_{sph,74} &= S_{sph,74}\underbrace{E_{44}^{-1}}_{c_{44}} + S_{sph,77}\underbrace{E_{74}^{-1}}_{e_{14}} + S_{sph,78}\underbrace{E_{84}^{-1}}_{e_{15}} \\ P_{sph,85} &= S_{sph,85}\underbrace{E_{55}^{-1}}_{c_{44}} + S_{sph,87}\underbrace{E_{75}^{-1}}_{e_{15}} + S_{sph,88}\underbrace{E_{85}^{-1}}_{-e_{14}} = -P_{sph,74} \\ P_{sph,47} &= P_{sph,74} \\ P_{sph,58} &= P_{sph,85} \end{aligned} \tag{4.14}$$

5 Structure Example - Bone

Bone material is mainly composed of collagen, hydroxyapatite and some cavities filled with isotonic water. The methods shown in chapter 3 are used to estimate material properties for bone in this chapter. The mixing composition of the used materials corresponds to the cortical part of a human femur, see Fritsch and Hellmich [15].

The bone structure varies not only between the cortical and the cancelous bone, but the local micro structure varies in its composition as well. The following calculations allow the estimation of the material properties of extravascular bone material, provided the composition of this material is known. The stated values in this chapter are given in the following units: $[c] = \mathrm{GPa}$, $[e] = \mathrm{C/m^2}$ and $[\kappa] = \mathrm{pF/m}$.

5.1 Hierarchic structure of bone

To estimate the properties of extravascular bone material, a five step approach is used. Each step combines multiple material phases to describe its homogenized structure.

Since extravascular bone material consist of extracellular bone matrix, also known as ultrastructure, which embeds small water filled inclusions called lacunae. At this point, the properties of water are known, but not these of the ultrastructure, which have to be estimated in a separate step.

The ultrastructure consists of mineralized collagen fibers and hydroxyapatite foam, which both have to be evaluated in a separate step. Lastly for the calculation of the properties of collagen fibers are the characteristics of wet collagen required, which can be gained by combining crosslinked collagen and water in the intermolecular space. Since the properties of the pure, unblended materials collagen, water and hydroxyapatite are known, no further homogenization steps are required.

An overview of the calculated materials and their steps is given in section 5.1. Naturally it is inevitable to begin the calculation at its smallest building block, which is wet collagen in the case of bone material, as shown in section 5.2.

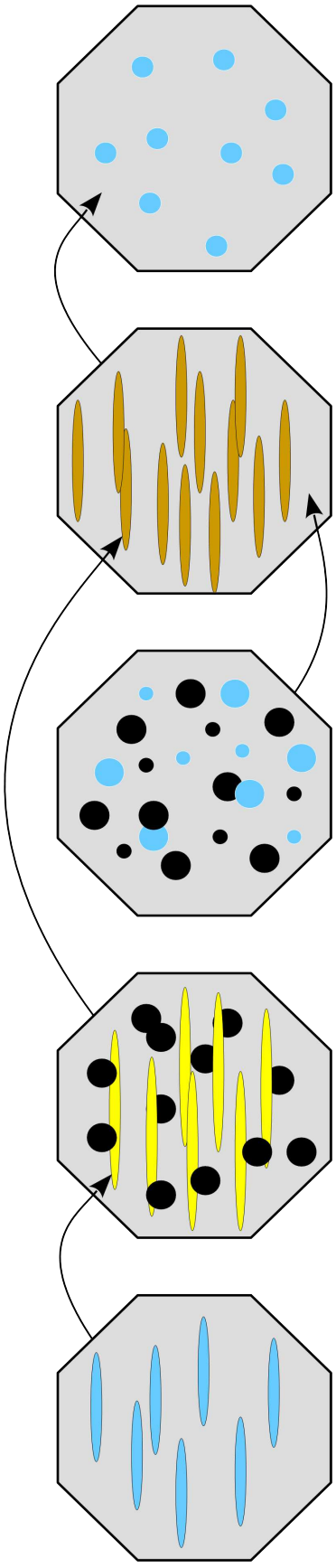

extravascular bone material

- characteristic length: $l_{exvas} \approx 100\mu m$
- matrix: ultrastructure, $\mathbb{M}_{ultra}$
- inclusions: spherical water filled lacunae, f_{lac}, $\mathbb{M}_{water}$

ultrastructure

- characteristic length: $l_{ultra} \approx 5 - 10\mu m$
- matrix: hydroxyapatite foam, $\mathbb{M}_{ef}$
- inclusions: cylindrical fibrils, f_{fib}, $\mathbb{M}_{fib}$

hydroxyapatite foam

- characteristic length: $l_{ef} \approx 100 - 500nm$
- intersecting phases:
  - spherical water filled space, f_{ic}, $\mathbb{M}_{water}$
  - spherical hydroxyapatite, f_{ha}, $\mathbb{M}_{ha}$

fibrils

- characteristic length: $l_{fib} \approx 100 - 500nm$
- intersecting phases:
  - cylindrical wet collagen, f_{wetcol}, $\mathbb{M}_{wetcol}$
  - spherical hydroxyapatite, f_{ha}, $\mathbb{M}_{ha}$

wet collagen

- characteristic length: $l_{wetcol} \approx 10nm$
- matrix: crosslinked collagen, $\mathbb{M}_{col}$
- inclusions: cylindrical water filled space, f_{im}, $\mathbb{M}_{water}$

Figure 5.1: Hierarchical structure of bone with the corresponding material phases.

5.2 Wet collagen

44% of the volume of the wet collagen consist of collagen. The remaining 56% are intermolecular space in a cylindrical shape filled with salt water. See Table B.1 for used material parameter.

Calculating a cylindrical Piezo-Eshelby tensor $\mathbf{S}_{cyl}^{col}$ and material parameters for wet collagen $\mathbf{M}_{wetcol}$ yields results as shown in Equation 5.3. The results are summarized in Table B.2.

$$\mathbf{S}_{cyl}^{col} = \begin{pmatrix} 0.68 & 0.04 & 0.30 & 0 & 0 & 0 & 0 & 0 & 0.0002 \\ 0.04 & 0.68 & 0.30 & 0 & 0 & 0 & 0 & 0 & 0.0002 \\ 0 & 0 & 0 & 0 & 0 & 0 & 0 & 0 & 0 \\ 0 & 0 & 0 & 0.50 & 0 & 0 & 0 & 0 & 0 \\ 0 & 0 & 0 & 0 & 0.50 & 0 & 0 & 0 & 0 \\ 0 & 0 & 0 & 0 & 0 & 0.64 & 0 & 0 & 0 \\ 0 & 0 & 0 & 0 & 0 & 0 & 0.50 & 0 & 0 \\ 0 & 0 & 0 & 0 & 0 & 0 & 0 & 0.50 & 0 \\ 0 & 0 & 0 & 0 & 0 & 0 & 0 & 0 & 0 \end{pmatrix} \tag{5.1}$$

$$\mathbf{P}_{cyl}^{col} = \begin{pmatrix} 0.07 & -0.027 & -9.9e-20 & 0 & 0 & 0 & 0 & 0 & -6.8e^{-21} \\ -0.027 & 0.07 & -1.1e-17 & 0 & 0 & 0 & 0 & 0 & -3.4e^{-21} \\ 0 & 0 & 0 & 0 & 0 & 0 & 0 & 0 & 0 \\ 0 & 0 & 0 & 0.15 & -1.7e^{-21} & 0 & -0.001 & 0.00055 & 0 \\ 0 & 0 & 0 & -1.7e^{-21} & 0.15 & 0 & 0.00055 & 0.001 & 0 \\ 0 & 0 & 0 & 0 & 0 & 0.19 & 0 & 0 & 0 \\ 0 & 0 & 0 & -0.001 & 0.00055 & 0 & -0.037 & 5.9e^{-22} & 0 \\ 0 & 0 & 0 & 0.00055 & 0.001 & 0 & 5.9e^{-22} & -0.037 & 0 \\ 0 & 0 & 0 & 0 & 0 & 0 & 0 & 0 & 0 \end{pmatrix} \tag{5.2}$$

$$\mathbf{M}_{wetcol} = \begin{pmatrix} 4.69 & 3.24 & 3.61 & 0 & 0 & 0 & 0 & 0 & 0.0014 \\ 3.24 & 4.69 & 3.61 & 0 & 0 & 0 & 0 & 0 & 0.0014 \\ 3.61 & 3.61 & 8.53 & 0 & 0 & 0 & 0 & 0 & 0.0049 \\ 0 & 0 & 0 & 0.93 & 0 & 0 & -0.03 & 0.01 & 0 \\ 0 & 0 & 0 & 0 & 0.93 & 0 & 0.01 & 0.03 & 0 \\ 0 & 0 & 0 & 0 & 0 & 0.73 & 0 & 0 & 0 \\ 0 & 0 & 0 & -0.03 & 0.01 & 0 & -44.86 & 0 & 0 \\ 0 & 0 & 0 & 0.01 & 0.03 & 0 & 0 & -44.86 & 0 \\ 0.0014 & 0.0014 & 0.0049 & 0 & 0 & 0 & 0 & 0 & -353.04 \end{pmatrix} \tag{5.3}$$

To get the above results, Equation 3.1 is used with the material properties $\mathbf{M}_{col}, \mathbf{M}_{water}$ and the respective volume fraction for the impurity $f_{im} = 56\%$ and for the collagen $f_{col} = 1 - f_{im} = 44\%$ and reads as in Equation 5.4a.

$$\begin{aligned}\mathbf{M}_{wetcol} = &\left(f_{col}\,\mathbf{M}_{col} + f_{im}\,\mathbf{M}_{water} \cdot \left[\mathbb{I} + \mathbf{P}^{col}_{cyl} \cdot (\mathbf{M}_{water} - \mathbf{M}_{col})\right]^{-1}\right) \\ &\cdot \left(f_{col}\,\mathbb{I} + f_{im} \cdot \left[\mathbb{I} + \mathbf{P}^{col}_{cyl} \cdot (\mathbf{M}_{water} - \mathbf{M}_{col})\right]^{-1}\right)^{-1}\end{aligned} \tag{5.4a}$$

$$\text{with} \quad \mathbf{P}^{col}_{cyl} = \mathbf{S}^{col}_{cyl} \cdot \mathbf{M}^{-1}_{col} \tag{5.4b}$$

$$\text{satisfying} \quad 1 = f_{col} + f_{im} \tag{5.4c}$$

5.3 Fibrils

The next step is to combine wet collagen with hydroxyapatite [15, fig. 3(b)]. The two phases build the material by intersecting geometries, leading to a implicit representation [20] of the desired properties, which is solved numerically in a stepwise approach by repeated calculations.

Starting point was an averaged material of wet collagen and hydroxyapatite chosen, as shown in Equation 5.5. Calculated with the material parameter for wet collagen and hydroxyapatite E_{wetcol}, E_{ha} and the corresponding volume fractions $f_{ha} = 29\%$ and $f_{wetcol} = 71\%$. [15]

$$\mathbf{M}^{starting\ matrix}_{fib} = f_{ha} \cdot \mathbf{M}_{ha} + f_{wetcol} \cdot \mathbf{M}_{wetcol} \tag{5.5}$$

The effective values are approached by iteration, as in

$$\begin{aligned}\mathbf{M}_{fib} = &\left(f_{ha}\,\mathbf{M}_{ha} \cdot (\mathbb{I} + \mathbf{P}^{fib}_{sph} \cdot (\mathbf{M}_{ha} - \mathbf{M}_{fib}))^{-1}\right. \\ &\left. + f_{wetcol}\,\mathbf{M}_{wetcol} \cdot (\mathbb{I} + \mathbf{P}^{fib}_{cyl} \cdot (\mathbf{M}_{wetcol} - \mathbf{M}_{fib}))^{-1}\right) \\ &\cdot \left(f_{ha}\,(\mathbb{I} + \mathbf{P}^{fib}_{sph} \cdot (\mathbf{M}_{ha} - \mathbf{M}_{fib}))^{-1}\right. \\ &\left. + f_{wetcol}\,(\mathbb{I} + \mathbf{P}^{fib}_{cyl} \cdot (\mathbf{M}_{wetcol} - \mathbf{M}_{fib}))^{-1}\right)^{-1}\end{aligned} \tag{5.6a}$$

$$\begin{aligned}\text{with} \quad \mathbf{P}^{fib}_{cyl} &= \mathbf{S}^{fib}_{cyl} \cdot \mathbf{M}^{-1}_{fib} \\ \mathbf{P}^{fib}_{sph} &= \mathbf{S}^{fib}_{sph} \cdot \mathbf{M}^{-1}_{fib}\end{aligned} \tag{5.6b}$$

Resulting in:

$$\mathbf{M}_{fib} = \begin{pmatrix} 8.20 & 4.76 & 5.24 & 0 & 0 & 0 & 0 & 0 & 5e^{-6} \\ 4.76 & 8.20 & 5.24 & 0 & 0 & 0 & 0 & 0 & 5e^{-6} \\ 5.23 & 5.23 & 16.86 & 0 & 0 & 0 & 0 & 0 & 2e^{-4} \\ 0 & 0 & 0 & 2.22 & -0.00 & 0 & -0.01 & 0.02 & 0 \\ 0 & 0 & 0 & 0.00 & 2.22 & 0 & 0.02 & 0.01 & 0 \\ 0 & 0 & 0 & 0 & 0 & 1.72 & 0 & 0 & 0 \\ 0 & 0 & 0 & -0.01 & 0.02 & 0 & -59.52 & 0.00 & 0 \\ 0 & 0 & 0 & 0.02 & 0.01 & 0 & -0.00 & -59.52 & 0 \\ 5e^{-6} & 5e^{-6} & 2e^{-4} & 0 & 0 & 0 & 0 & 0 & -257.12 \end{pmatrix} \tag{5.7}$$

5.4 Hydroxyapatite foam

Analog to the fibrils, hydroxyapatite foam is built by spherical hydroxyapatite and spheric intercrystalline space, which is assumed to be filled with water. The volume fraction of hydroxyapatite is $f_{ha} = 68\%$. The characteristics of the foam in the extravascular space E_{ef} are shown in Equation 5.8.

$$\mathbf{M}_{ef} = \begin{pmatrix} 51.64 & 17.87 & 17.87 & 0 & 0 & 0 & 0 & 0 & 0 \\ 17.87 & 51.64 & 17.87 & 0 & 0 & 0 & 0 & 0 & 0 \\ 17.87 & 17.87 & 51.64 & 0 & 0 & 0 & 0 & 0 & 0 \\ 0 & 0 & 0 & 16.89 & 0 & 0 & 0.30 & 0 & 0 \\ 0 & 0 & 0 & 0 & 16.89 & 0 & 0 & -0.30 & 0 \\ 0 & 0 & 0 & 0 & 0 & 16.89 & 0 & 0 & 0 \\ 0 & 0 & 0 & 0.30 & 0 & 0 & -205.90 & 0.00 & 0 \\ 0 & 0 & 0 & 0 & -0.30 & 0 & -0.00 & -205.90 & 0 \\ 0 & 0 & 0 & 0 & 0 & 0 & 0 & 0 & -197.50 \end{pmatrix} \tag{5.8}$$

To calculate the material properties of the hydroxyapatite foam in the extrafibrillar space, the same self consistent scheme as for the fibrils is used, which reads as in Equation 5.10a. The starting matrix is calculated as in Equation 5.9. Again this is an implicit formulation can be numerically solved with multiple iterations.

$$\mathbf{M}_{ef}^{starting\ matrix} = f_{ha} \cdot \mathbf{M}_{ha} + f_{water} \cdot \mathbf{M}_{water} \tag{5.9}$$

$$\begin{aligned}\mathbf{M}_{ef} = &\Big(f_{ha}\,\mathbf{M}_{ha}\cdot(\mathbb{I}+\mathbf{P}^{ef}_{sph}\cdot(\mathbf{M}_{ha}-\mathbf{M}_{ef}))^{-1}\\ &+f_{water}\,\mathbf{M}_{water}\cdot(\mathbb{I}+\mathbf{P}^{ef}_{cyl}\cdot(\mathbf{M}_{water}-\mathbf{M}_{ef}))^{-1}\Big)\\ &\cdot\Big(f_{ha}(\mathbb{I}+\mathbf{P}^{ef}_{sph}\cdot(\mathbf{M}_{ha}-\mathbf{M}_{ef}))^{-1}\\ &+f_{water}\,(\mathbb{I}+\mathbf{P}^{ef}_{cyl}\cdot(\mathbf{M}_{water}-\mathbf{M}_{ef}))^{-1}\Big)^{-1}\end{aligned} \tag{5.10a}$$

$$\text{with}\quad \mathbf{P}^{ef}_{sph} = \mathbf{S}^{ef}_{sph}\cdot\mathbf{M}^{-1}_{ef} \tag{5.10b}$$

$$\text{satisfying}\quad 1 = f_{ha}+f_{water} \tag{5.10c}$$

5.5 Ultrastructure

Calculating the extracellular bone matrix, consisting of 53% fibrils, embedded in hydroxyapatite, results in the following values, shown in Equation 5.11.

$$\mathbf{P}^{ef}_{cyl} = \begin{pmatrix} 0.015 & -0.005 & 1.2e^{-15} & 0 & 0 & 0 & 0 & 0 & -7.2e^{-23}\\ -0.005 & 0.015 & 1.2e^{-15} & 0 & 0 & 0 & 0 & 0 & -7.2e^{-23}\\ 0 & 0 & 0 & 0 & 0 & 0 & 0 & 0 & 0\\ 0 & 0 & 0 & 0.015 & 0 & 0 & 2.2e^{-5} & -2.8e^{-16} & 0\\ 0 & 0 & 0 & 0 & 0.015 & 0 & -2.8e^{-16} & -2.2e^{-5} & 0\\ 0 & 0 & 0 & 0 & 0 & 0.02 & 0 & 0 & 0\\ 0 & 0 & 0 & 2.2e^{-5} & -2.8e^{-16} & 0 & -0.0024 & -1.7e^{-9} & 0\\ 0 & 0 & 0 & -2.8e^{-16} & -2.2e^{-5} & 0 & 1.7e^{-9} & -0.0024 & 0\\ 0 & 0 & 0 & 0 & 0 & 0 & 0 & 0 & 0 \end{pmatrix} \tag{5.11}$$

$$\mathbf{M}_{ultra} = \begin{pmatrix} 20.30 & 8.86 & 8.86 & 0 & 0 & 0 & 0 & 0 & 4e^{-6}\\ 8.86 & 20.30 & 8.86 & 0 & 0 & 0 & 0 & 0 & 4e^{-6}\\ 8.85 & 8.85 & 32.17 & 0 & 0 & 0 & 0 & 0 & 9e^{-5}\\ 0 & 0 & 0 & 7.12 & -0.00 & 0 & 0.08 & 0.01 & 0\\ 0 & 0 & 0 & 0.00 & 7.12 & 0 & 0.01 & -0.08 & 0\\ 0 & 0 & 0 & 0 & 0 & 5.72 & 0 & 0 & 0\\ 0 & 0 & 0 & 0.08 & 0.01 & 0 & -112.76 & 0 & 0\\ 0 & 0 & 0 & 0.01 & -0.08 & 0 & 0 & -112.76 & 0\\ 4e^{-6} & 4e^{-6} & 9e^{-5} & 0 & 0 & 0 & 0 & 0 & -229.10 \end{pmatrix} \tag{5.12}$$

To calculate the cylindrically shaped fibrils in the hydroxyapatite foam, Equation 5.13a is used. The volume fraction of the fibrils $f_{fib} = 53\%$ and the volume fraction of the hydroxyapatite foam f_{ef} is required.

$$\mathbf{M}_{ultra} = \left(f_{ef}\,\mathbf{M}_{ef} + f_{fib}\,\mathbf{M}_{fib} \cdot \left[\mathbb{I} + \mathbf{P}^{ef}_{cyl} \cdot (\mathbf{M}_{fib} - \mathbf{M}_{ef})\right]^{-1} \right) \cdot \left(f_{ef}\,\mathbb{I} + f_{fib} \cdot \left[\mathbb{I} + \mathbf{P}^{ef}_{cyl} \cdot (\mathbf{M}_{fib} - \mathbf{M}_{ef})\right]^{-1} \right)^{-1} \tag{5.13a}$$

$$\text{with} \quad \mathbf{P}^{ef}_{cyl} = \mathbf{S}^{ef}_{cyl} \cdot \mathbf{M}^{-1}_{ef} \tag{5.13b}$$

$$\text{satisfying} \quad 1 = f_{ef} + f_{fib} \tag{5.13c}$$

5.6 Extravascular bone material

To estimate extravascular bone material, the ultrastructure is assumed to be interspersed with cavities and channels, filled with substances close to isotonic water. The volume fraction of the lacunae equals $f_{lac} = 2.06\%$ [15], [21].

$$\mathbf{P}^{ultra}_{sph} = \begin{pmatrix} 0.0311 & -0.0082 & -0.0055 & 0 & 0 & 0 & 0 & 0 & -1.6e^{-7} \\ -0.0082 & 0.0311 & -0.0055 & 0 & 0 & 0 & 0 & 0 & -1.6e^{-7} \\ -0.0055 & -0.0055 & 0.0207 & 0 & 0 & 0 & 0 & 0 & 5.4e^{-7} \\ 0 & 0 & 0 & 0.0339 & 0 & 0 & 2.9e^{-06} & 1.5e^{-6} & 0 \\ 0 & 0 & 0 & 0 & 0.0339 & 0 & 1.5e^{-6} & -2.9e^{-6} & 0 \\ 0 & 0 & 0 & 0 & 0 & 0.0393 & 0 & 0 & 0 \\ 0 & 0 & 0 & 2.9e^{-6} & 1.5e^{-6} & 0 & -0.0025 & -5.6e^{-9} & 0 \\ 0 & 0 & 0 & 1.5e^{-6} & -2.9e^{-6} & 0 & 5.6e^{-9} & -0.0025 & 0 \\ -1.6e^{-7} & -1.6e^{-7} & 5.4e^{-7} & 0 & 0 & 0 & 0 & 0 & -0.0019 \end{pmatrix} \tag{5.14}$$

$$\mathbf{M}_{exvas} = \begin{pmatrix} 19.60 & 8.58 & 8.60 & 0 & 0 & 0 & 0 & 0 & -6e^{-5} \\ 8.58 & 19.60 & 8.60 & 0 & 0 & 0 & 0 & 0 & -6e^{-5} \\ 8.59 & 8.59 & 30.87 & 0 & 0 & 0 & 0 & 0 & -9e^{-5} \\ 0 & 0 & 0 & 6.84 & -0.00 & 0 & 0.08 & 0.01 & 0 \\ 0 & 0 & 0 & 0.00 & 6.84 & 0 & 0.01 & -0.08 & 0 \\ 0 & 0 & 0 & 0 & 0 & 5.51 & 0 & 0 & 0 \\ 0 & 0 & 0 & 0.08 & 0.01 & 0 & -117.40 & 0 & 0 \\ 0 & 0 & 0 & 0.01 & -0.08 & 0 & 0 & -117.40 & 0 \\ -6e^{-5} & -6e^{-5} & -9e^{-5} & 0 & 0 & 0 & 0 & 0 & -233.78 \end{pmatrix} \tag{5.15}$$

The extravascular material, using the ultrastructure as matrix with spherical water inclusions, can be calculated like wet collagen or the ultrastructure. The corresponding equation is given explicitly in Equation 5.16a.

$$\begin{aligned}\mathbf{M}_{exvas} = &\left(f_{ultra}\,\mathbf{M}_{ultra} + f_{lac}\,\mathbf{M}_{water}\cdot\left[\mathbb{I} + \mathbf{P}_{sph}^{ultra}\cdot(\mathbf{M}_{water} - \mathbf{M}_{ultra})\right]^{-1}\right)\\ &\cdot\left(f_{ultra}\,\mathbb{I} + f_{lac}\cdot\left[\mathbb{I} + \mathbf{P}_{sph}^{ultra}\cdot(\mathbf{M}_{water} - \mathbf{M}_{ultra})\right]^{-1}\right)^{-1}\end{aligned} \tag{5.16a}$$

$$\text{with}\quad \mathbf{P}_{sph}^{ultra} = S_{sph}^{ultra}\cdot\mathbf{M}_{ultra}^{-1} \tag{5.16b}$$

$$\text{satisfying}\quad 1 = f_{ultra} + f_{lac} \tag{5.16c}$$

6 Piezoelectric impact on cells in bone tissue

The majority of the cells in the bone tissue are osteocytes, which make up to 95% of all bone cells, and are embedded in the extracellular matrix [4]. Osteocytes play a major role in the remodeling of the bone matrix to adapt to mechanical load, whether this sensing or only promoting a mechanical signal, which can happen with chemical messenger substances or by the piezoelectric effect in the fluids of the lacunar-canicular network [7].

It has been shown, that the extracellular matrix interacts with the osteocytes, governing cell growth, differentiation and its signaling behavior [8]. This effect is most likely dependent to the surface binding sites of the cell, to attach to the collagen in the extracellular matrix as well as its gradient of calcium ions. While it is known that osteocytes play a major role in bone regeneration [22] and there are also attempts to use piezoelectric materials as bone scaffolds [23], it would be interesting to know on which scale of size and effect the piezoelectricity from the bone matrix is and if it can affect the processes in living bone.

The dendritic like protuberances bestow the osteocytes with a star shaped cell form with a cell body diameter of roughly 5-20µm [24]. Therefore it makes sense to compare it to the extracellular bone material from the simulation (see section 5.5, which has a characteristic length of 5-10µm [15].

Patch-clamp experiments confirmed voltage dependent channels in bone cell membranes [25], as well as channels which work only in a specific area of electrical stimulation. In a model system free from external electric fields, we can assume the electric polarization P as in Equation 6.1.

$$P = e \cdot \varepsilon \tag{6.1}$$

Assuming the cell membrane as a capacitor with an area dependent capacitance $C_{el} \approx 10\frac{\mathrm{mF}}{\mathrm{m}^2}$ [26], a polarization P of about $500\frac{\mu\mathrm{C}}{\mathrm{m}^2}$ is needed to create a voltage difference U of about 50mV.

$$U = \frac{P}{C_{el}} \tag{6.2}$$

In case an osteocyte is attached at the x_{12} plane of the extracellular ultrastructure, a strain of about $\varepsilon_{33} \approx 5.6$ is required to create the 50mV pulse, which can be obtained by a strain of about $\sigma \approx 150$GPa. Of course this is far more than bone material can stand without breaking (about 170-220MPa for compact bone [27]). Additionally, since this is the main load bearing direction, the areas close to the osteocyte might be disencumbered or load shielded.

The more important case might be an osteocyte placed laterally to the load bearing structure. In this example (see Equation 6.3), a shear strain of about $\varepsilon_{13} \approx 0.58\%$ is required to create the same electrical potential, which can be obtained by a shear stress of $\sigma_{13} \approx 260$MPa, see Equation 3.11. However, this exceeds the maximum shear strength of human bone by far (about 50-70MPa [28]), therefore it is unlikely, that piezoelectric stimuli from the bone matrix is the leading sensory input for the bone building mechanisms.

$$\begin{aligned} P_1 &= e_{14}\varepsilon_{13} + e_{15}\varepsilon_{23} \\ \sigma_{13} &= c_{44}\varepsilon_{13} \end{aligned} \tag{6.3}$$

$$\text{assuming } \vec{E} = \vec{0}$$

7 Analysis of various volume fractions in bone materials

The properties of bone vary significantly between different bones. Also the bone composition in animals varies from species to species, but the structure always remains the same. This chapter investigates the effect on changed volume fractions and how this affects the simulation results.

7.1 Wet collagen

The density collagen structures may vary, yielding different phase fractions of water in it. Figure 7.1 and Figure 7.2 show the effect of various amounts of water in collagen.

Naturally the stiffness and piezoelectric properties decrease with an increasing amount of included water. Hereby can be observed that the decrease is not linear. Another noteworthy detail is in c_{44} and c_{66}, these moduli start and end at the same values, but show a different behavior for the mixed material.

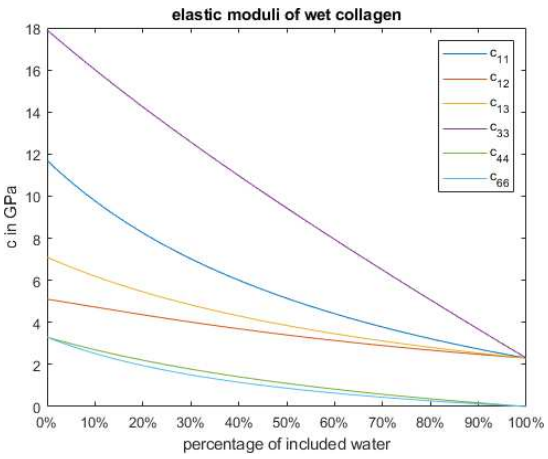

Figure 7.1: Elastic moduli of wet collagen, including various amounts of water.

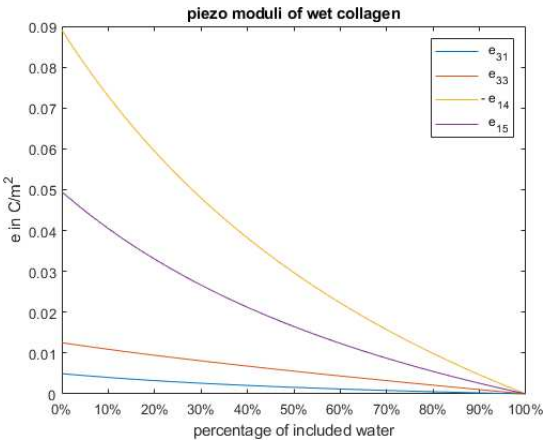

Figure 7.2: Piezo moduli of wet collagen, including various amounts of water.

7.2 Fibrils

In this section, the important moduli of fibrils are shown, dependent on the volume fractions of hydroxyapatite and wet collagen, as shown in Equation 5.1.

The mechanical properties showing the typical kinked characteristic, when varying the mixing ratio of wet collagen and hydroxyapatite. The same is valid for the piezo modulus e_{14}, which is connected to the shear strain on the material. The moduli e_{31}, e_{32}, e_{33}, which are connected to the normal strain, are in a subordinate role.

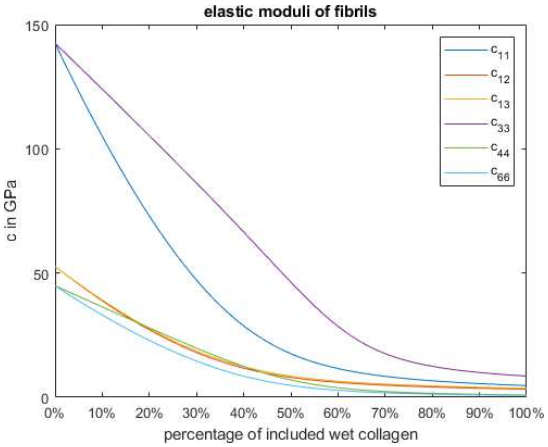

Figure 7.3: Elastic moduli of fibrils, including various amounts of wet collagen.

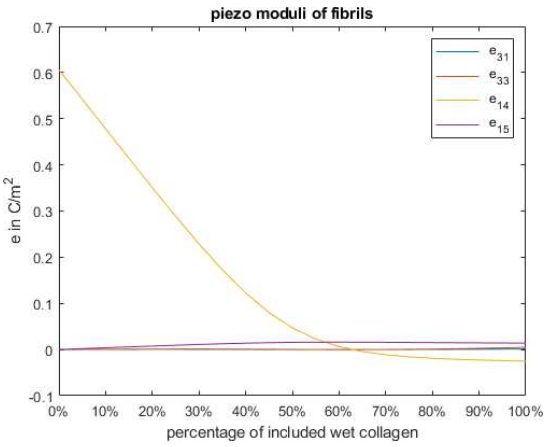

Figure 7.4: Piezo moduli of fibrils, including various amounts of wet collagen.

In experimental approaches to determine piezoelectric properties of fibrils, single fibrils from tendons were examined with a piezoresponse force microscope [29]. These measurements indicate a piezoelectric coefficient $d_{15} \approx 1 \frac{\mathrm{pC}}{\mathrm{N}}$, but some uncertainties of some material parameters and the grade of mineralization remain.

The piezoelectric coefficients d can be obtained as in Equation 7.1 and the results are shown in Figure 7.5. The simulation shows a fine correlation to the experimental results for fibrils with a higher grade of mineralization.

$$\boldsymbol{d} = \frac{\boldsymbol{e}}{\mathbf{c}} \tag{7.1}$$

$$[d] = \frac{\mathrm{C}}{\mathrm{N}} = \frac{\mathrm{m}}{\mathrm{V}}$$

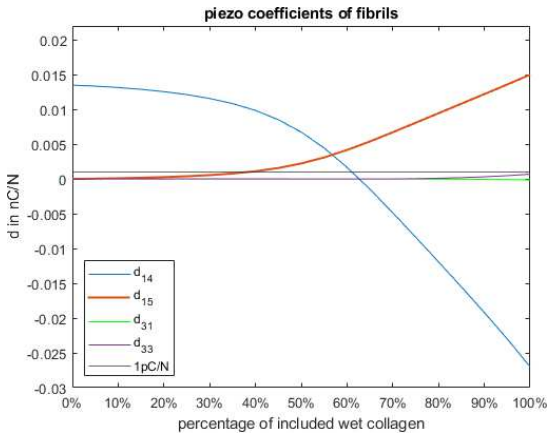

Figure 7.5: Piezoelectric coefficient of fibrils, including various amounts of wet collagen.

7.3 Hydroxyapatite foam

This section features the important moduli of hydroxyapatite foam, dependent on the volume fractions of hydroxyapatite and water, see Table B.1 for the initial material parameters.

The stiffness of the hydroxyapatite foam is decreasing significantly with an increasing amount of water, till there is more water than hydroxyapatite. Beyond this point, the homogenized material seems to be more of a liquid containing hydroxyapatite particles. The same observation is valid for the piezoelectric modulus e_14. Since neither water nor hydroxyapatite have noteworthy piezoelectric properties in the other directions, they remain close to zero.

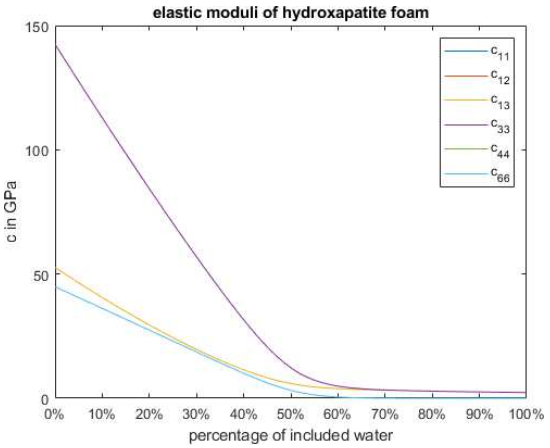

Figure 7.6: Elastic moduli of hydroxyapatite foam, including various amounts of water.

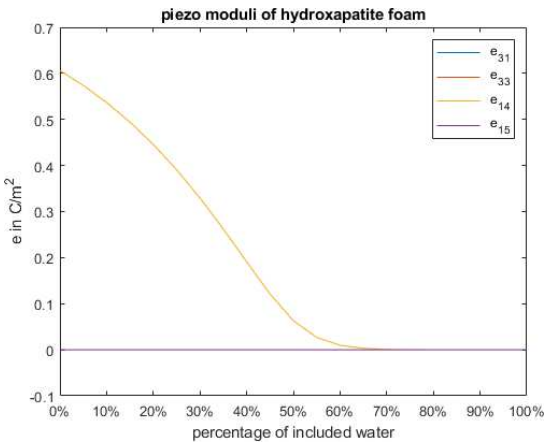

Figure 7.7: Piezo moduli of hydroxyapatite foam, including various amounts of water.

7.4 Ultrastructure

In this section, the important moduli of the ultrastructure are shown, dependent on the volume fractions of hydroxyapatite foam (as in Equation 5.8) and fibrils (as shown in Equation 5.7).

Since hydroxyapatite is much stiffer than fibrils, it is not surprising, that the stiffness will decrease with a rising amount of fibrils. Also the typical kinked behavior can be observed for the mechanic moduli as well as for the piezo moduli.

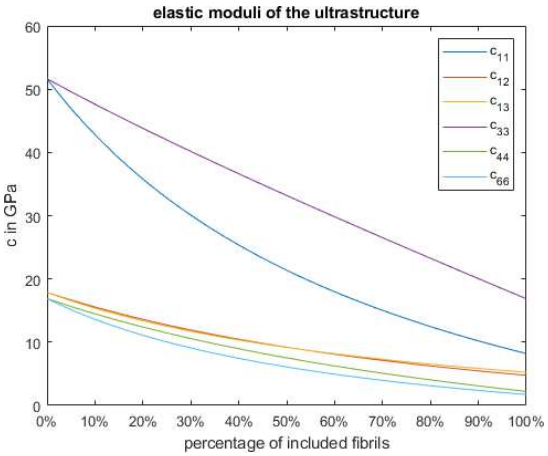

Figure 7.8: Elastic moduli of the ultrastructure, including various amounts of fibrils.

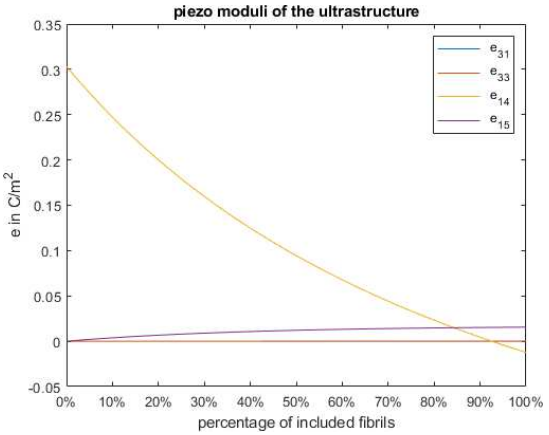

Figure 7.9: Piezo moduli of the ultrastructure, including various amounts of fibrils.

7.5 Extravascular bone material

In this section, the important moduli of the ultrastructure are shown, dependent on the volume fractions of the ultrastructure (as in Equation 5.11) and the water filled lacunae, see Figure 7.10 and Figure 7.11.

All elastic moduli show a slightly kinked behavior in this analysis. Unlike the piezo modulus e_{14}, which appears to decrease almost linearly to the point, where the homogenized extravascular bone material is made up by more than 50% of water.

At this point it should be mentioned that the volume taken in by lacunae is usually very low compared to this simulated example. In section 5.6 was a volume fraction of $f_{lac} = 2.06\%$ assumed for a human femur.

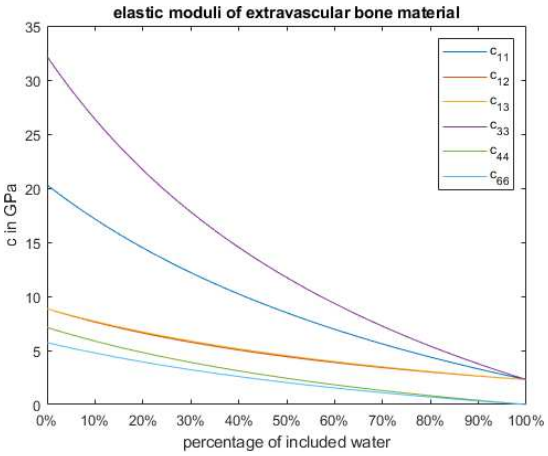

Figure 7.10: Elastic moduli of extravascular bone material, including various amounts of water.

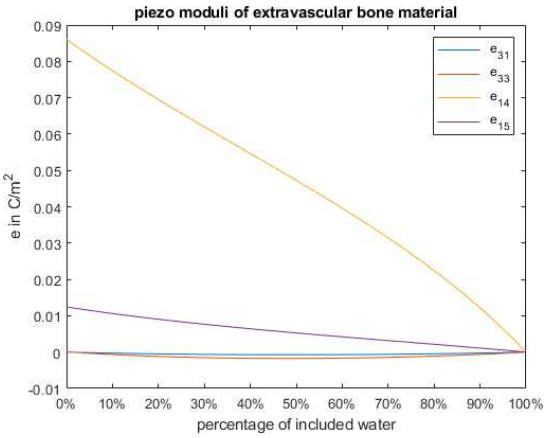

Figure 7.11: Piezo moduli of extravascular bone material, including various amounts of water.

7.6 Dried collagen

Before measurements, bone is often dried or prepared somehow. This of course affects the amount of water in the homogenized material, but the amount of collagen will remain the same. The following example is wet collagen with a volume fraction of 44% collagen, as in section 5.2, dried, meaning the water is replaced by air.

Since neither water nor air has piezoelectric properties, these values will not change while the collagen is drying. The same applies to the shear moduli c_{44} and c_{66}, which will also stay unchanged, as depicted in Figure 7.12 and Figure 7.13.

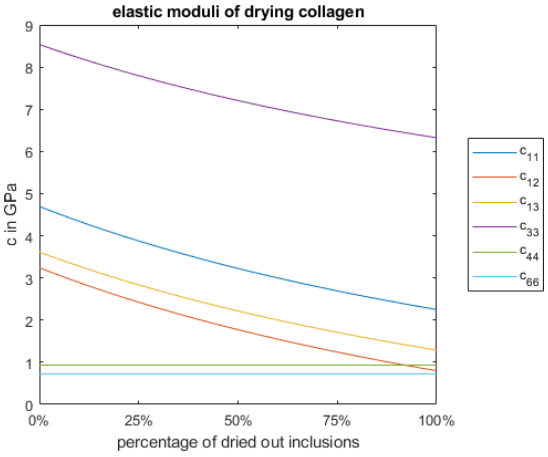

Figure 7.12: Elastic moduli of drying collagen. The material values decrease, while the water is replaced by air.

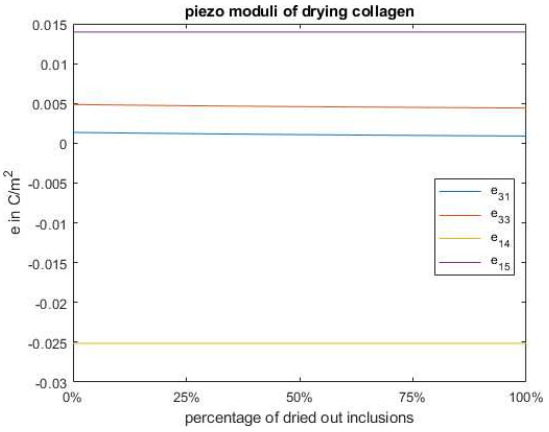

Figure 7.13: Piezo moduli of drying collagen. Since only collagen has piezoelectric properties, these will not change, when the water is replaced by air. The shear moduli are unaffected by this.

8 Inclusion geometry

This chapter will examine the influence of the inclusion geometry on the effective material parameters. The previously discussed inclusions have either been perfectly spherical, or right circular cylindrical. Compressed or otherwise deformed inclusion geometries have an impact on the resulting material properties, especially on the piezoelectric part, because the main part of piezoelectricity in collagen and hydroxyapatite are in the shear stress depending parameters e_{14} and e_{15}.

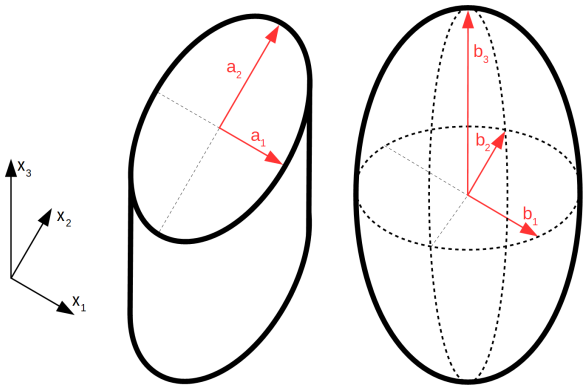

Figure 8.1: Schemata of the used inclusion geometries. The cylinder and the ellipsoid are oriented like the coordinate system, to avoid an unnecessary transformation.

However, changing the aspect ratio α will lead to an anisotropic material, this has to be considered in the calculation of the Eshelby tensor. Therefore simplifications for isotropic or transversely isotropic materials do not apply in this case. The symmetries from isotropic or transversely isotropic materials will not apply in anisotropic materials, as in Equation 8.1. Changing the aspect ratio β will not affect transversal isotropy, since it varies the geometry normal to the isotropy plane, as in Equation 8.3. See Appendix C for a Piezo-Eshelby tensor with an anisotropic matrix material.

$$\begin{aligned} &c_{11} \neq c_{22} \neq c_{33} \rightarrow \text{anisotropic} \\ &c_{12} \neq c_{13} \neq c_{23} \\ &c_{44} \neq c_{55} \neq c_{66} \end{aligned} \tag{8.1}$$

8.1 Deformed cylinder in wet collagen

The elliptic base of the cylinder is spanned by the semi-axes a_1 and a_2. Their proportion gives the aspect ratio α, as in Equation 8.2 [17, section 6]. In the following example, wet collagen with the same properties as in section 5.2, is computed, but with Piezo-Eshelby tensors, featuring various aspect ratios, as shown in Figure 8.2.

$$\alpha = \frac{a_1}{a_2} \tag{8.2}$$

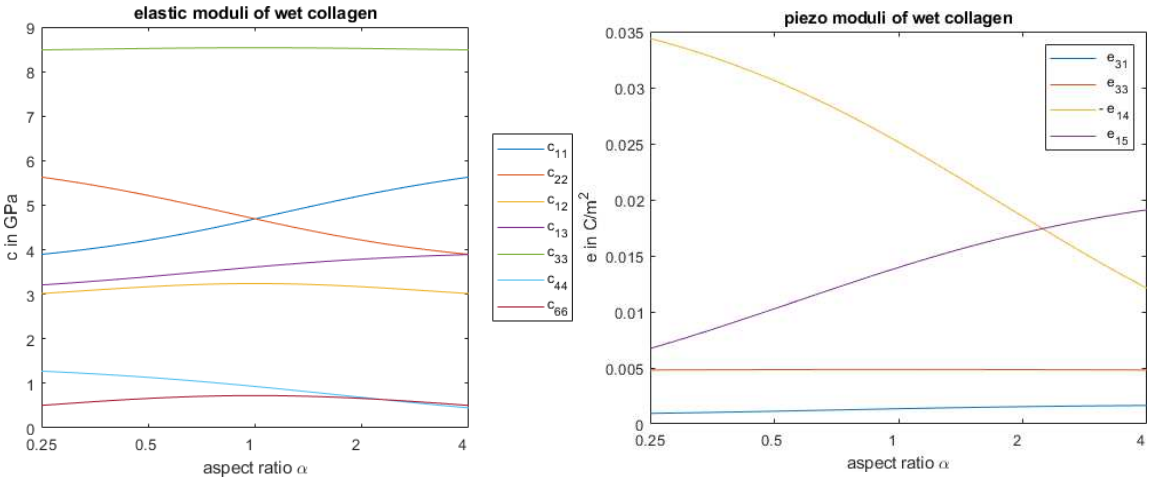

Figure 8.2: Elastic and piezo moduli of wet collagen, consisting of 44% collagen and 56% water, with various aspect ratios α. As expected, the bulk moduli along the cylinder axis c_{33}, e_{33} are almost unaffected by the change. The moduli in the varied directions a_1, a_2 seem centrally symmetric around $\alpha = 1$, particularly good to see at c_{11} and c_{22}. But the shear dependent values, as e_{14} and e_{15}, are strongly affected by the change of the aspect ratio α.

8.2 Changed inclusions in fibrils

To estimate material properties for fibrils, both the cylindrical and spherical inclusion geometries are needed. The definition for the aspect ratio α for the elliptic-cylindrical inclusion remains the same as in the previous section. The spheroid gets deformed to an ellipsoid by varying the semi-axis b_3, which is aligned with the cylinder axis and the axis x_3 from the coordinate system [18].

$$\begin{aligned} b_1 &= b_2 \\ \beta &= \frac{b_1}{b_3} = \frac{b_2}{b_3} \end{aligned} \tag{8.3}$$

Homogenizing a transversely isotropic matrix with an inclusion, which may be isotropic or transversely isotropic with the same orientation, yields a transversely isotropic material, if the inclusion is symmetric in the plane of isotropy. Using a deformed inclusion with an aspect ratio $\alpha \neq 1$ will result in an anisotropic material. Since the use of the self-consistent scheme requires multiple iterations to estimate the properties of a homogenized material, a calculation for an anisotropic Piezo-Eshelby tensor is needed, which is given in Appendix C.

Analog to data from wet collagen, see section 8.1, the shape of the inclusion cylinder has no effect on moduli such as c_{33}, as depicted in Figure 8.6.However, since the piezo shear moduli are not symmetric, some changes in e_{33} can be seen for slim hydroxyapatite inclusions, as in 8.10.

The data also shows an increase in the elasticity for the parameter c_{12} for flat disc-like hydroxyapatite inclusions, which can obviously be expected, when visualized with regard to the material properties. More interesting is the immense increase of the parameter c_{11} to almost its triple value, if the combination of flat cylinders and ellipsoids with an aspect ratio of 4 are given.

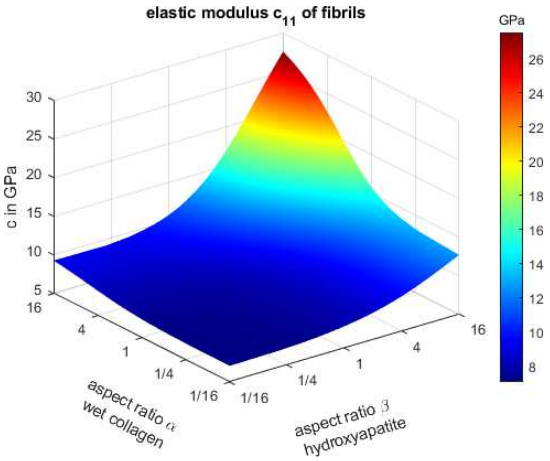

Figure 8.3: Elastic modulus c_{11} of fibrils with different inclusion geometries, showing the highest values for disc like hydroxyapatite inclusions and wet collagen stretched in the x_1 direction.

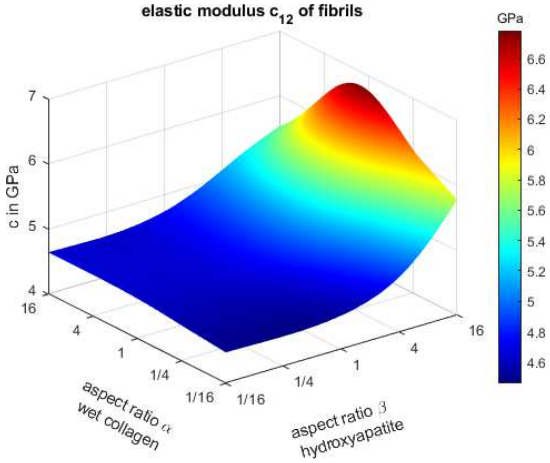

Figure 8.4: Elastic modulus c_{12} of fibrils with different inclusion geometries, showing the highest values for disc like hydroxyapatite and cylindric wet collagen inclusions.

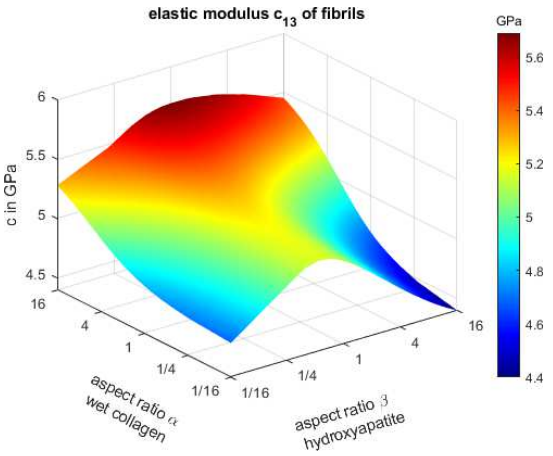

Figure 8.5: Elastic modulus c_{13} of fibrils with different inclusion geometries, showing the highest values for spherical hydroxyapatite inclusions and wet collagen stretched in the x_1 direction.

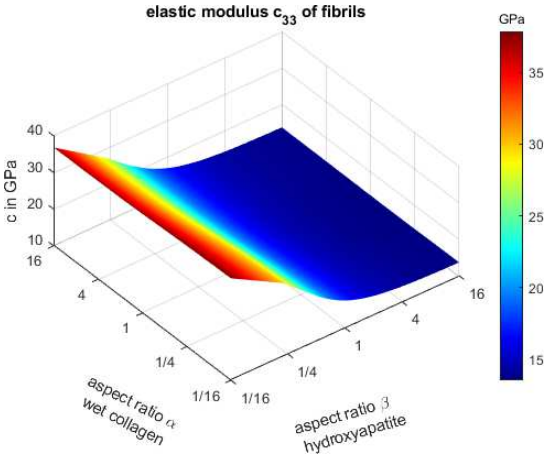

Figure 8.6: Elastic modulus c_{33} of fibrils with different inclusion geometries, showing the highest values for slim, needle like hydroxyapatite inclusions. Since this parameter is on the axis of the cylindrical wet collagen inclusions, its footprint geometry has no impact on this modulus.

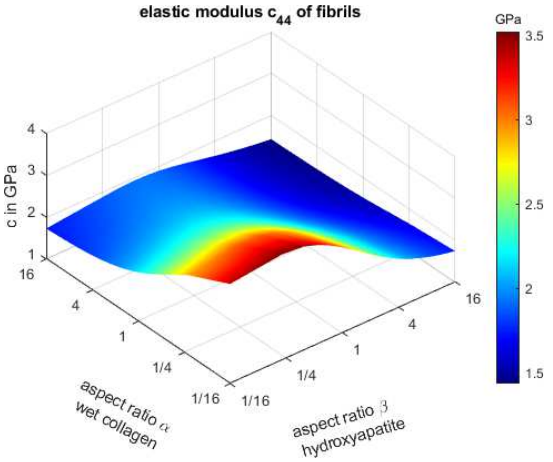

Figure 8.7: Elastic modulus c_{44} of fibrils with different inclusion geometries, showing slightly higher values for slim hydroxyapatite inclusions with wet collagen stretched in the x_2 direction.

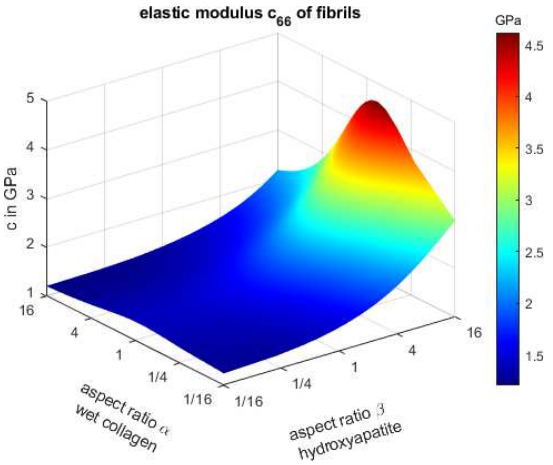

Figure 8.8: Elastic modulus c_{66} of fibrils with different inclusion geometries, showing the highest values for disc like hydroxyapatite and cylindric wet collagen inclusions.

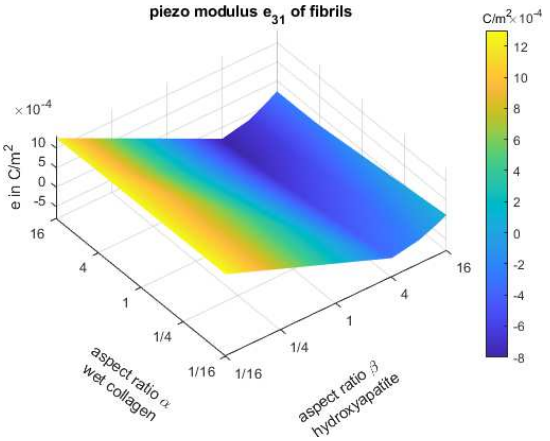

Figure 8.9: Piezo modulus e_{31} of fibrils with different inclusion geometries, showing higher values for slim hydroxyapatite inclusions. This non continuous behavior is a result from the interaction with the other moduli.

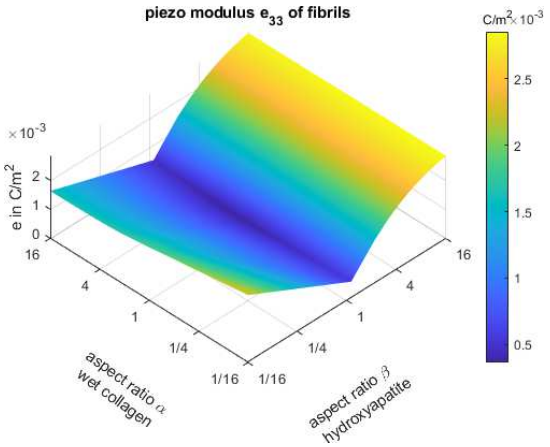

Figure 8.10: Piezo modulus e_{33} of fibrils with different inclusion geometries, showing higher values for slim hydroxyapatite inclusions oriented in the x_3 direction.

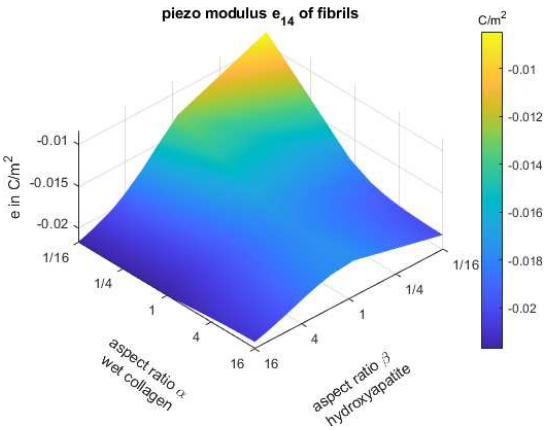

Figure 8.11: Piezo modulus e_{14} of fibrils with different inclusion geometries, showing significantly higher values for slim hydroxyapatite inclusions with collagen stretched in the x_2 direction.

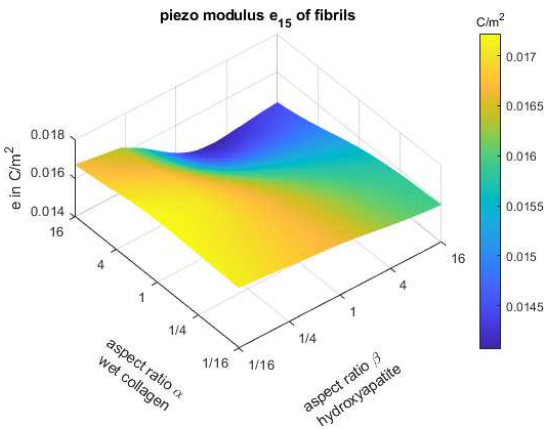

Figure 8.12: Piezo modulus e_{15} of fibrils with different inclusion geometries, showing higher values for slim hydroxyapatite inclusions.

8.3 Changed inclusions in hydroxyapatite foam

Other than fibrils, hydroxyapatite foam consist of two interlocking spherical phases. Results for close to spherical inclusions are shown in Figure 8.13 to Figure 8.19.

Since hydroxyapatite has only two non-zero piezo moduli $e_{14} = -e_{25} \neq 0$ and water does not have any piezoelectric characteristics, the homogenized foam possesses only this shear dependent piezo property. No new piezo characteristics are added by this homogenization step, therefore e_{31}, e_{33} and e_{15} are zero.

Concerning the elastic moduli, the most important load bearing direction in the bone is oriented along the x_3 axis, which makes c_{33} an important value for resisting a compressive load along the bone axis. As in fiber reinforced materials, the stiffness modulus c_{33} profits from long filament like inclusions structures.

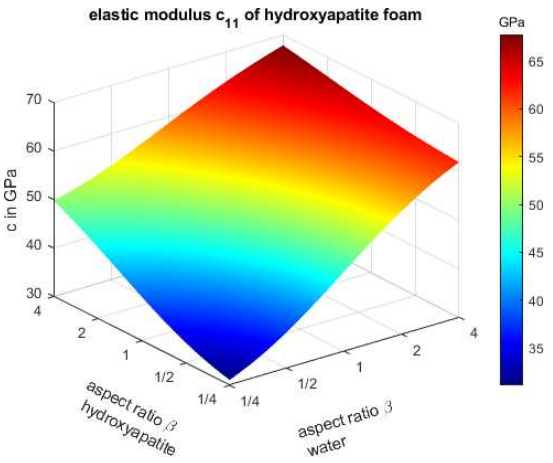

Figure 8.13: Elastic modulus c_{11} of hydroxyapatite foam with different inclusion geometries. This value is the highest, when both inclusion phases have a disc like geometry in the x_3 direction. Therefore it is evident, that this material can resist lateral forces better.

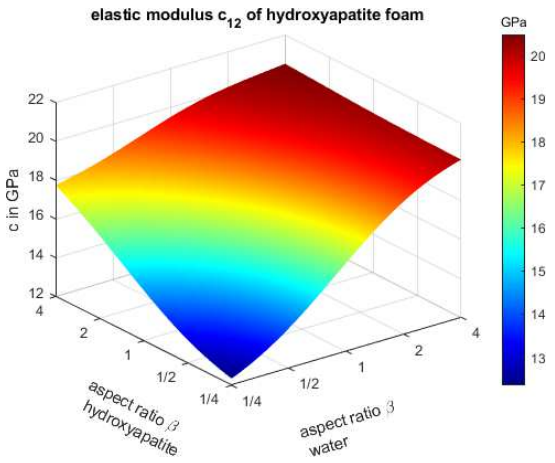

Figure 8.14: Elastic modulus c_{12} of hydroxyapatite foam with different inclusion geometries, showing higher values for flat disc like inclusions of both phases. However the shape of the usually liquid water inclusion has an higher impact than the geometry of the hydroxyapatite.

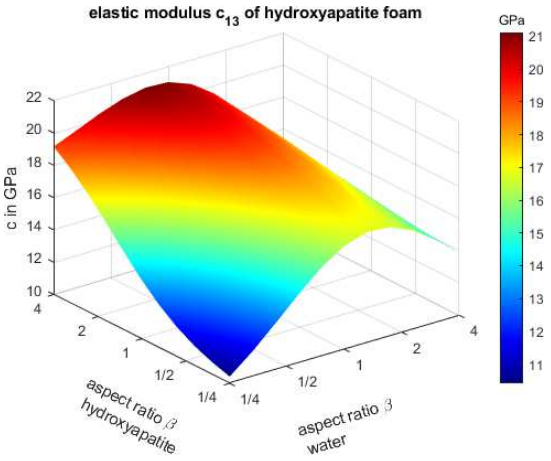

Figure 8.15: Elastic modulus c_{13} of hydroxyapatite foam with different inclusion geometries, showing the highest values for spherical water inclusions and disc shaped hydroxyapatite inclusions.

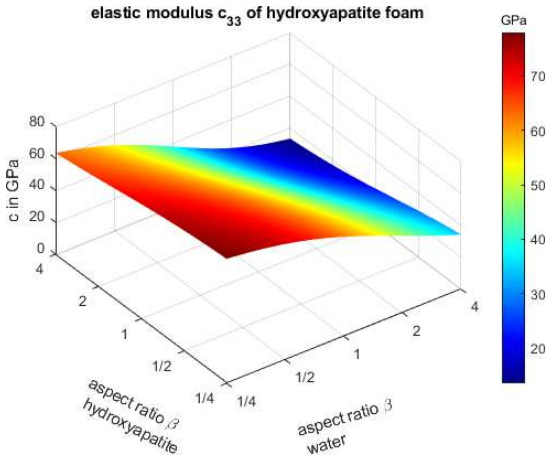

Figure 8.16: Elastic modulus c_{33} of hydroxyapatite foam with different inclusion geometries showing the highest value for slim needle like inclusions of both phases.

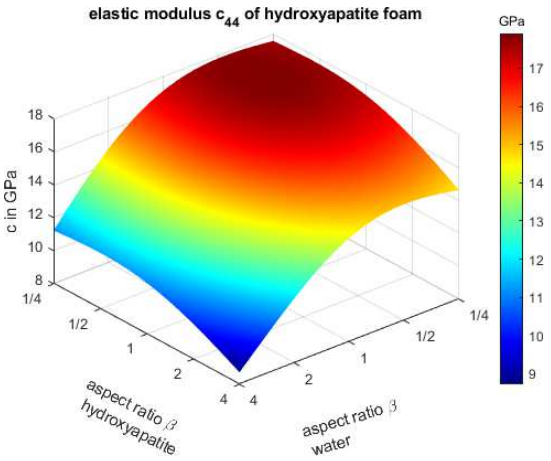

Figure 8.17: Elastic modulus c_{44} of hydroxyapatite foam with different inclusion geometries, showing the highest value for slim needle like inclusions of both phases.

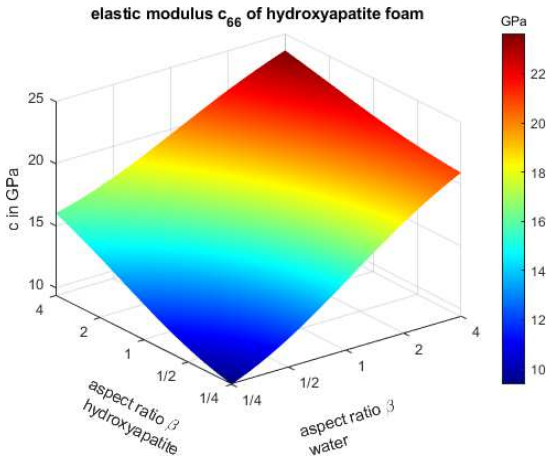

Figure 8.18: Elastic modulus c_{66} of hydroxyapatite foam with different inclusion geometries, showing the highest value for flat disc like inclusions of both phases. Therefore the behavior is contrary from the other elastic shear modulus c_{44}.

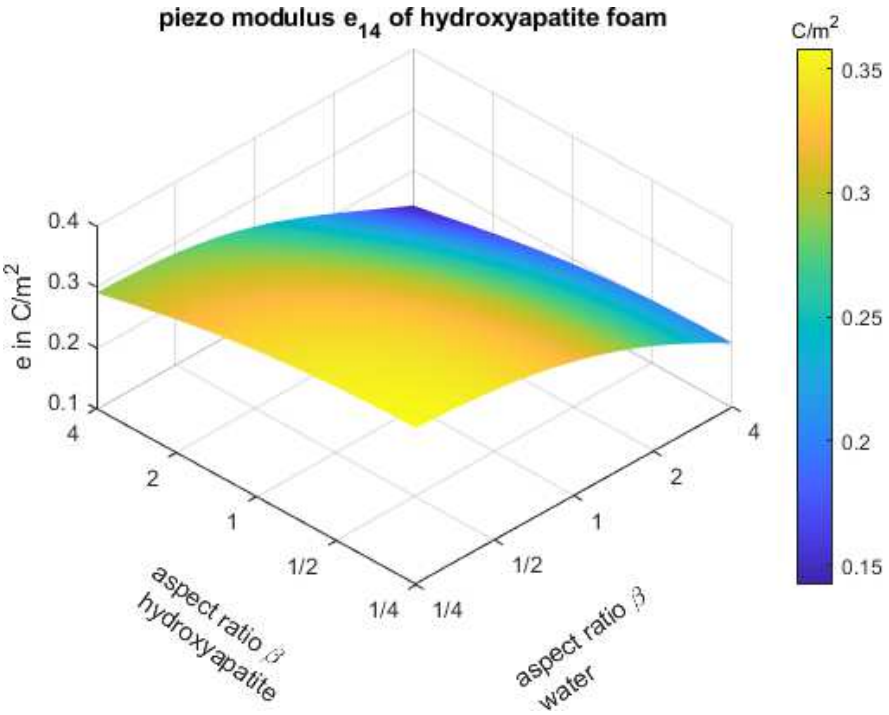

Figure 8.19: Piezo modulus e_{14} of hydroxyapatite foam with different inclusion geometries, showing the highest values for slim inclusion geometries of both material phases.

8.4 Deformed fibrils in the ultrastructure

As expected, the deformation of fibrils shows a similar behavior to the deformed cylindrical inclusions in wet collagen, see section 8.1. For a clearer diagram, the centrally symmetric moduli are not displayed in Figure 8.20.

Since the fibrils are the main factor for the piezoelectric effect, the geometry dependent change of the piezo modulus e_{14} is easy to spot. The moduli e_{31} and e_{33} have almost no influence on the material, since they are much lower.

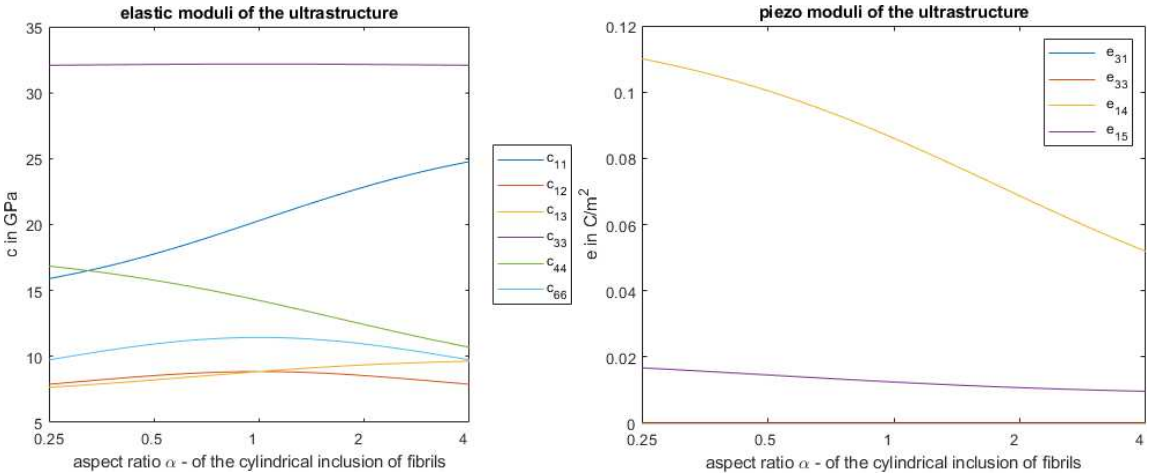

Figure 8.20: Elastic and piezo moduli of the ultrastructure, consisting of 53% fibrils and 47% hydroxyapatite foam, with various aspect ratios α.

Another effect of the deformed fibrils is, that the previously used symmetries $e_{15} = e_{24}$ and $e_{14} = -e_{25}$ are not valid anymore. This is only true for symmetric inclusion geometries, as for $\alpha = 1$, as depicted in Figure 8.21.

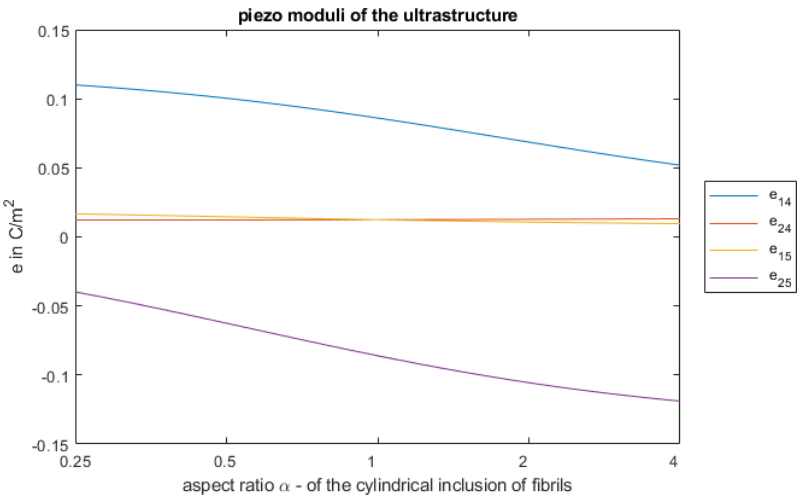

Figure 8.21: Asymmetric behavior of piezo moduli in the ultrastructure.

8.5 Deformed lacunae in extravascular bone material

A change of the aspect ratio β of a spherical inclusion affects the estimated material parameter in an obviously different way. The example in Figure 8.22 does not change the symmetry in the isotropic axes x_1, x_2 but describes a change in the x_3 axis. However, this might be the most interesting inclusion to study, because lacunae as well as channels in the bone come in a big variety of forms and shapes.

It seems that slim inclusions, with $\beta < 1$, have only a minor impact on the stiffness and piezoelectric properties of the extravascular bone material. However, flat disc shaped inclusions are significantly weakening the material strength and lowering the important piezo modulus e_{31}.

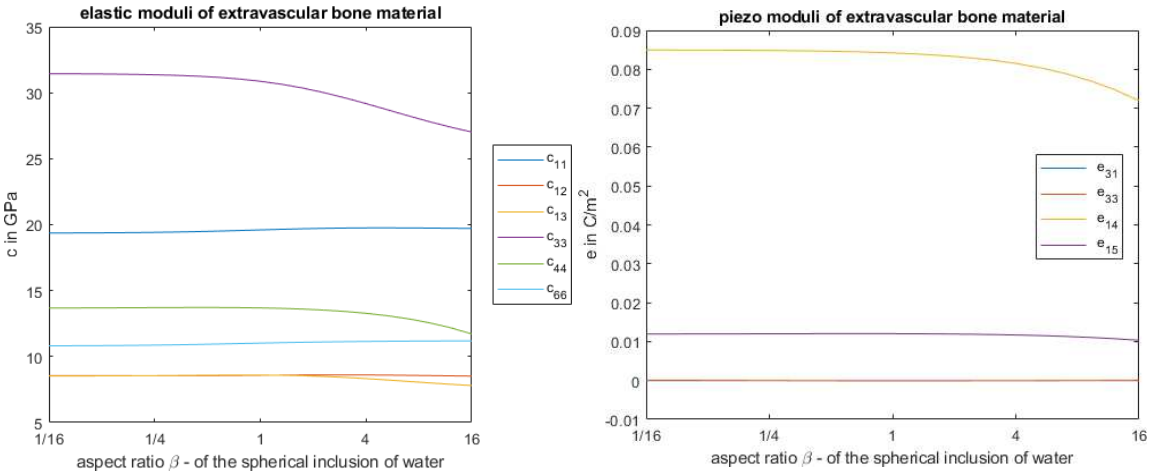

Figure 8.22: Elastic and piezo moduli of extravascular bone material, with a volume fraction of 2.06% with water filled lacunae, with various aspect ratios β.

9 Structure Example - Tooth

Teeth show the highest mineral density in the human body, and are, like bone, composed of materials with piezoelectric properties, which make examining this material further worth it. The main components of tooth material, enamel and dentin, vary from the outside to the pulp in composition of the building materials and its orientation [30], similar to cortical and trabecular bone.

9.1 Enamel

The outermost layer of the teeth represents the part of the human body with the highest mineral concentration. The hydroxyapatite crystals make up about 95% of the total volume, attached to about 2% collagen and interspersed with 3% water [31]. The hydroxyapatite crystals come in a rod-like and plate-like structure [32], varying their composition between the outside of the tooth to dentin.

$$\mathbf{M}_{enamel} = \begin{pmatrix} 107.23 & 38.19 & 36.75 & 0 & 0 & 0 & 0 & 0 & -0.05 \\ 38.19 & 107.23 & 36.75 & 0 & 0 & 0 & 0 & 0 & -0.05 \\ 35.93 & 35.93 & 109.31 & 0 & 0 & 0 & 0 & 0 & -0.015 \\ 0 & 0 & 0 & 26.61 & 0 & 0 & 0.32 & 0.02 & 0 \\ 0 & 0 & 0 & 0 & 26.61 & 0 & 0.02 & -0.32 & 0 \\ 0 & 0 & 0 & 0 & 0 & 34.52 & 0 & 0 & 0 \\ 0 & 0 & 0 & 0.32 & 0.02 & 0 & -106.21 & 0 & 0 \\ 0 & 0 & 0 & 0.02 & -0.32 & 0 & 0 & -106.21 & 0 \\ -0.05 & -0.05 & -0.015 & 0 & 0 & 0 & 0 & 0 & -97.91 \end{pmatrix} \tag{9.1}$$

Equation 9.1 shows the result for enamel on the surface of a tooth, consisting of 95% hydroxyapatite (40% as plates $\beta = 0.125$, 60% as rods $\beta = 8$), 3% water in spherical solutions and 2% collagen. These results match references values from measurements very well [33].

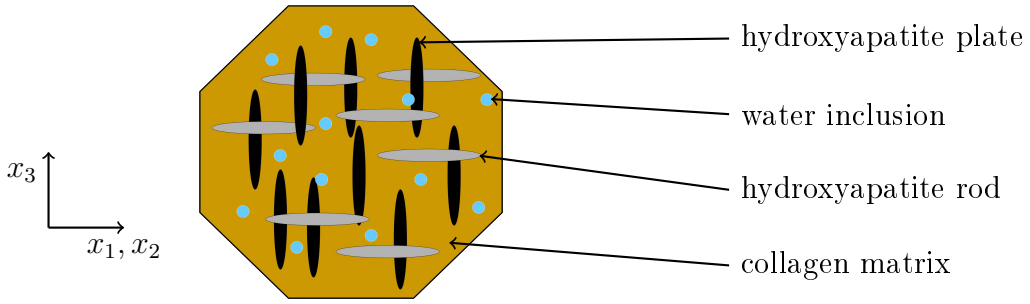

Figure 9.1: Schema depicting the material phases in enamel.

9.1.1 Phases in enamel

The above described model consists of the following phases on a collagen matrix and was calculated as shown in Equation 3.1. The phases from Equation 9.2, depicted in Figure 9.1, and the prior mentioned equation lead to the same homogenization rule as in Equation 9.3.

$$s, r = \begin{Bmatrix} \text{collagen}, & \text{as matrix} \\ \text{hydroxyapatite}, & \text{spherical } \beta = \frac{1}{8} \text{ (plate)} \\ \text{hydroxyapatite}, & \text{spherical } \beta = 8 \text{ (rod)} \\ \text{water}, & \text{spherical } \beta = 1 \end{Bmatrix} \tag{9.2}$$

$$\begin{aligned} \mathbf{M}_{enamel} = &\{f_{col}\mathbf{M}_{col} + f_{rod}\mathbf{M}_{ha} \cdot (\mathbb{I} + \mathbf{P}^{col}_{rod} \cdot (\mathbf{M}_{ha} - \mathbf{M}_{col}))^{-1} \\ &+ f_{plate}\mathbf{M}_{ha} \cdot (\mathbb{I} + \mathbf{P}^{col}_{plate} \cdot (\mathbf{M}_{ha} - \mathbf{M}_{col}))^{-1} \\ &+ f_{water}\mathbf{M}_{water} \cdot (\mathbb{I} + \mathbf{P}^{col}_{water} \cdot (\mathbf{M}_{water} - \mathbf{M}_{col}))^{-1}\} \\ &\cdot \{f_{col}\mathbb{I} + f_{rod}(\mathbb{I} + \mathbf{P}^{col}_{rod} \cdot (\mathbf{M}_{ha} - \mathbf{M}_{col}))^{-1} \\ &+ f_{plate}(\mathbb{I} + \mathbf{P}^{col}_{plate} \cdot (\mathbf{M}_{ha} - \mathbf{M}_{col}))^{-1} \\ &+ f_{water}(\mathbb{I} + \mathbf{P}^{col}_{water} \cdot (\mathbf{M}_{water} - \mathbf{M}_{col}))^{-1}\}^{-1} \end{aligned} \tag{9.3}$$

$$\text{satisfying } \quad 1 = f_{col} + f_{rod} + f_{plate} + f_{water} \tag{9.4}$$

9.1.2 Elasticity of enamel

The simulation shows, that the combination of both geometries influences the elasticity moduli of enamel dependent on the direction and increase of its overall value. A higher amount of plates increases the elasticity in the normal direction of the tooth surface, while a higher concentration of so called enamel-rods increase the elasticity in the transverse directions.

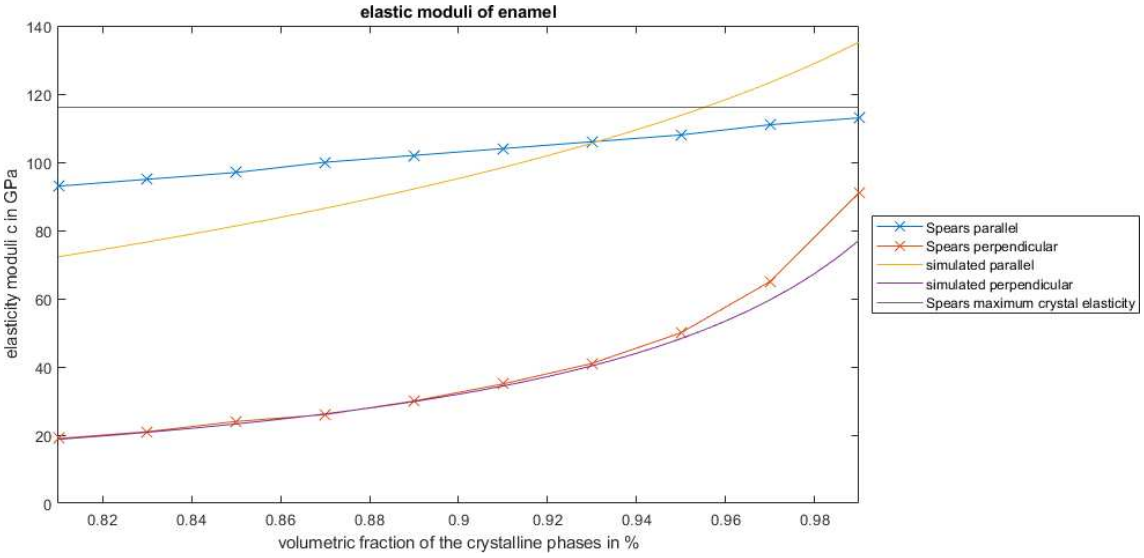

Figure 9.2: Spears researched the effect of the mineral-volume fraction in the direction of the crystal axis and transverse to it [33]. The simulation for plate-like hydroxyapatite inclusions shows almost the same results for the elastic modulus in transverse direction, but has a slightly higher slope for the elastic modulus parallel to the crystal orientation. However Spears assumed a maximum elasticity for the crystal of about 116GPa, the simulation uses the same values as in Table B.1 ($c_{33} = 142\text{GPa}$). Further refining these phase properties might lead to better results.

9.1.3 Piezoelectric properties of enamel

The piezoelectric effect in enamel can not be calculated this easily. Reyes-Gasga, Galindo-Mentle, Brès, *et al.* [34] inspected various areas of the tooth enamel and measured its piezoelectric properties. He measured the piezoelectric effect in a single enamel grain, resulting in $d = 15.86 \pm 0.89\text{pC/N}$ which are matched by the results from the simulation above, see Equation 9.1.

$$d_{33} = \frac{e_{33}}{c_{33}} \tag{9.5}$$
$$d_{33} = \frac{1.84}{109.31 \cdot 10^9} = 16,56\text{pC/N}$$

However, the overall piezoelectric effect of enamel is lower due to the merged enamel grains with different orientation. But the estimation of the properties of a single enamel grain with this multiscale estimation might be a good starting point to estimate the overall properties.

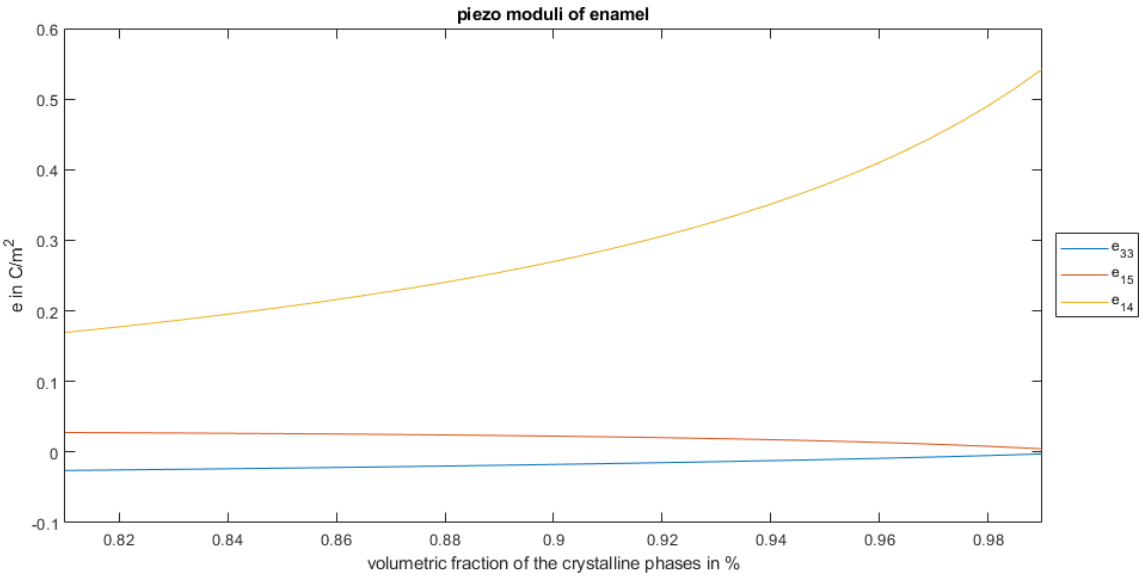

Figure 9.3: For the same material composition as in Figure 9.2, enamel shows a rise in e_{33} and e_{14} for an increasing amount of crystalline volume fractions. The other moduli e_{15} shows an insignificant decrease and e_{11} (not shown in this graphic) is almost unaffected by the change of the volume fractions.

9.2 Dentin

Under the enamel coat lies the less mineralized dentin. Just as enamel, but unlike bone, it is not vascularized but shows a great variety of composition and orientation of its building components. Summed up, the dentin composition has a high portion of water, which lies between 20% and 25% in volume, about 40% to 45% mineral material and the remaining 30% is the organic matrix [35, table 1].

9.2.1 Structure of dentin

Similar to bone material, a two step approach was used to estimate dentin. First the spherical hydroxyapatite crystals were added to the collagen matrix and on a bigger size scale were the spherical, water filled holes included. This structure can also be observed via scanning electron microscope [36]. With the volume fractions given above, the simulation results are shown in Figure 9.7 and Figure 9.5.

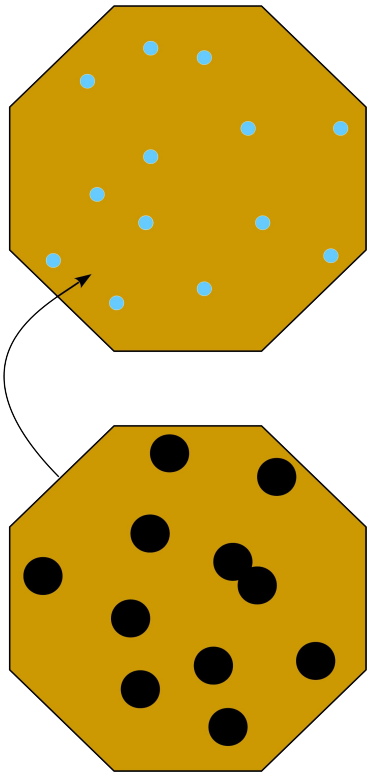

dentin

- matrix: mineralized collagen, $\mathbb{M}_{mc}$
- inclusions: spherical water inclusions, f_{water}, $\mathbb{M}_{water}$

mineralized collagen

- matrix: collagen, $\mathbb{M}_{col}$
- inclusions: spherical hydroxyapatite, f_{ha}, $\mathbb{M}_{ha}$

Figure 9.4: Hierarchical structure of dentin with the corresponding material phases.

9.2.2 Piezoelectric properties of dentin

For the piezoelectric part, dentin shows significant lower piezo moduli e than enamel, but the piezoelectric coefficients d (see Equation 9.5) is higher than in enamel, because the lower elasticity moduli play their part in this equation. This result fits the corresponding measurements [34, table 1&2], but again raises the question, whether the organic or the inorganic part of a composite material has the bigger impact on the overall piezoelectricity.

Many comparative studies test dentin with organic material against dentin, where the organic parts have been removed and therefore have a much smaller piezoelectric coefficient d. But the previous calculations result in higher piezo moduli e for compositions with higher mineral content, therefore the drop of the piezoelectric coefficient d, when removing the organic material, might be, because the material gets stiffer and d always has to be considered together with a force ($[d] = \frac{C}{N}$).

Measurements on human teeth, which had been treated with alcohol or formaldehyde and later dried, yielded much lower results for the piezoelectric coefficients [37]. These measurement yielded a piezoelectric coefficient from $11.7\frac{\text{fC}}{\text{N}}$ to $63.4\frac{\text{fC}}{\text{N}}$[1], whereby the simulation results yield values from $72\frac{\text{fC}}{\text{N}}$ to $91\frac{\text{fC}}{\text{N}}$ for bulk coefficient $d_{31} = d_{32}$. The shear coefficients d_{14}, d_{15} show much higher values anyway.

[1] 1 statCoulomb $\approx 3.33564 \cdot 10^{-1}$C, 1 dyne$= 10^{-5}$N

Another study on horse dentin reported a piezoelectric coefficient of $d_{33} = 3\frac{\text{fC}}{\text{N}}$ [38], again far below the calculated values for d_{33} from $218\frac{\text{fC}}{\text{N}}$ to $362\frac{\text{fC}}{\text{N}}$. Most likely these simulation results are valid for a single grain of dentin, rather than for the macroscopic composition of it.

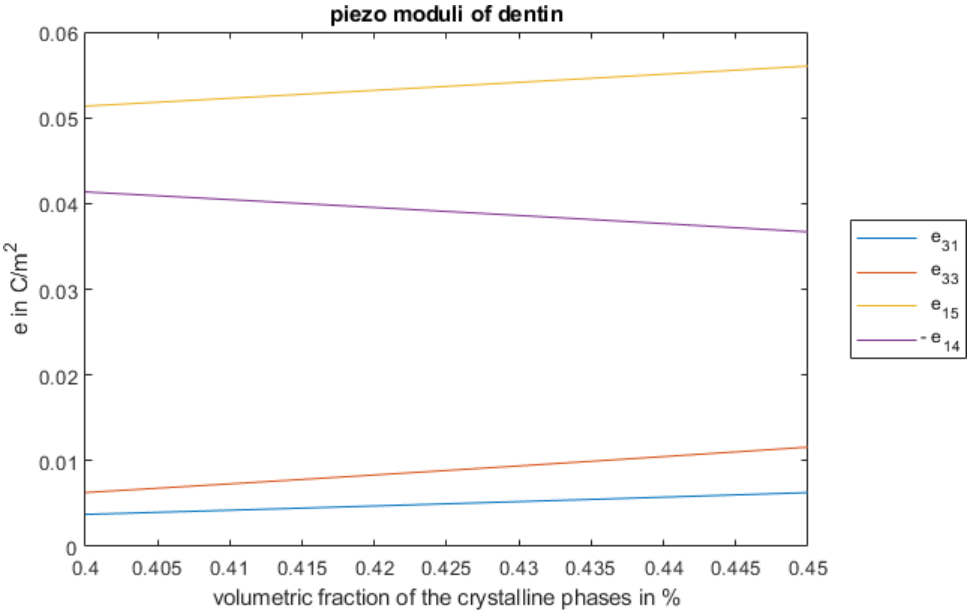

Figure 9.5: Piezo moduli of dentin with various amount of mineralization.

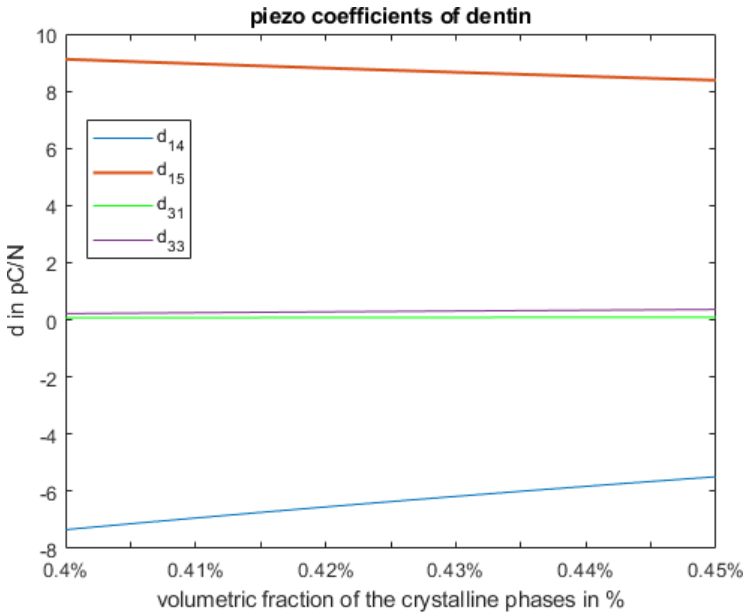

Figure 9.6: Piezo coefficient of dentin with various amount of mineralization.

9.2.3 Elasticity of dentin

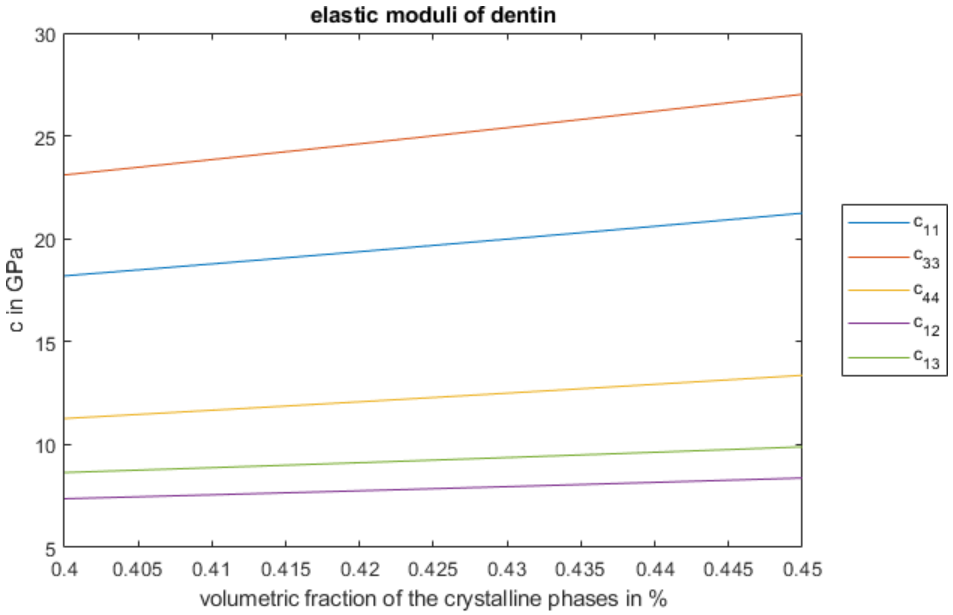

Figure 9.7: Elastic moduli of dentin with various amount of mineralization.

Various measurements of dentin yield results for the elastic bulk moduli in the range from 17GPa up to 30GPa, in rare cases over 40GPa [32, table 4]. These results are matched by the bulk moduli from the simulation, which cover a range from 18GPa to 27GPa in this very narrow defined scope for a mineralization from 40% to 45% percent.

9.3 Possible improvements on this estimation

Since enamel and dentin appear to have some grain like structure, it might be useful to append another homogenization step with the same phases but different orientations. For this, however, insight on the statistical distribution of the grains is needed. The mechanical properties will not be strongly affected, since the moduli are similar in all three axes, but they might improve the results for the piezoelectric parameter.

Another improvement might be made on the exact material composition. Since it is usually mentioned in reports which animal the specimen was taken from, this allows the statistical comparison of different species, but does not give any insight on the material composition of the probe. The simulation results can surely be improved with more knowledge on the exact material and structural composition of dentin and enamel on the various locations in a tooth.

10 | Conclusion

This document presented two methods to estimate a material's properties, which have been homogenized from multiple different material phases. Additionally, the required mathematical methods and the Eshelby tensor for solving the homonymous inclusion problem were introduced.

Further, a way to calculate a Piezo-Eshelby tensor, and a respective Piezo-Hill tensor to solve the homogenization problem, depending on the inclusion geometry was presented. This not only includes the application of already existing Piezo-Eshelby tensors, but also the consideration of additional piezo moduli, therefore allowing to handle more multifarious material properties.

Using the introduced methods, material examples for bone, tooth-enamel and dentin were calculated, yielding results close to macroscopic measurements, and therefore validating the applied method. The used simulation parameter are stated in the respective chapters, together with the depicted structural hierarchy the simulated material consists of.

Attempting to show the possibilities of the homogenization method, multiple material and geometric parameters have been changed, to describe different and in some cases more complex material structures and predict their behavior. This includes to inspect similar materials with different mixing proportions of their substructures or with changed inclusion geometries. Also an exchange of sub-phase materials and the therefore changed properties in the macroscopic material, like in a drying process, can be described.

Lastly, it was shown, that the direct piezoelectric effect of the extracellular matrix is very unlikely to effect osteocytes and their bone building behavior, connoting that there must be other physical effects governing the bone physiology. This was done by inspecting the calculated material properties and their possible interaction with the cell membranes of osteocytes and their voltage depending membrane channels.

A | List of used symbols

Following variables are used in this document. Chapter specific parameter are explained in their respective section.

c_{ij}	specific elastic modulus [Pa]
$\mathbb{C}$	macroscopic stiffness tensor, elastic moduli in fourth-order tensor representation [Pa]
$\mathbf{C}$	macroscopic stiffness tensor, elastic moduli in second-order tensor representation [Pa]
$\mathbb{c}$	microscopic stiffness tensor, elastic moduli in fourth-order tensor representation [Pa]
$\mathbf{c}$	microscopic stiffness tensor, elastic moduli in second-order tensor representation [Pa]
d	piezoelectric coefficient $\left[\frac{\mathrm{C}}{\mathrm{N}}\right] = \left[\frac{\mathrm{m}}{\mathrm{V}}\right]$
$\vec{D}$	electric displacement $\left[\frac{\mathrm{As}}{\mathrm{m}^2}\right]$
$\boldsymbol{\mathcal{E}}$	macroscopic mechanical strain
ε	microscopic mechanical strain
$\vec{\varepsilon}$	mechanical strain represented as first-order tensor
e_{ij}	specific piezoelectric modulus $\left[\frac{\mathrm{C}}{\mathrm{m}^2}\right]$
$\boldsymbol{e}$	piezoelectric moduli in third or second-order tensor representation $\left[\frac{\mathrm{C}}{\mathrm{m}^2}\right]$
E	electric field strength $\left[\frac{\mathrm{V}}{\mathrm{m}}\right]$
f	volume fractions
$\mathbb{I}$	unity tensor, represented as 9×9 identity matrix as second-order tensor
κ_{ij}	specific dielectric modulus $\left[\frac{\mathrm{F}}{\mathrm{m}}\right]$
κ	dielectric moduli in second-order tensor representation $\left[\frac{\mathrm{F}}{\mathrm{m}}\right]$
$\boldsymbol{K}$	macroscopic dielectric moduli $\left[\frac{\mathrm{F}}{\mathrm{m}}\right]$
$\mathbb{M}$	electromechanical coupling moduli, combination of c, e, κ [13, eq. 8]
$\mathbf{M}$	electromechanical coupling moduli as a second-order tensor

$\mathbb{P}$	Piezo-Hill tensor, fourth-order tensor
$\mathbf{P}$	Piezo-Hill tensor, second-order tensor in Kelvin-Mandel representation
P_{MnAb}	specific value of the fourth-order Piezo-Hill tensor, with $n, b \in \{1, 2, 3\}$ and $M, A \in \{1, 2, 3, 4\}$
P_{ij}	specific value of the second-order Piezo-Hill tensor, with $i, j \in \mathbb{N}[1, 9]$
Σ	macroscopic mechanical stress $\left[\frac{\mathrm{N}}{\mathrm{m}^2}\right]$
σ	microscopic mechanical stress $\left[\frac{\mathrm{N}}{\mathrm{m}^2}\right]$
$\mathbb{S}$	Piezo-Eshelby tensor, fourth-order tensor
$\mathbf{S}$	Piezo-Eshelby tensor, second-order tensor in Kelvin-Mandel representation
S_{MnAb}	specific value of the fourth-order Piezo-Eshelby tensor, with $n, b \in \{1, 2, 3\}$ and $M, A \in \{1, 2, 3, 4\}$
S_{ij}	specific value of the second-order Piezo-Eshelby tensor, with $i, j \in \mathbb{N}[1, 9]$
x_i	directions in the three dimensional room, with $i \in \{1, 2, 3\}$
y_i	directions of the inclusion half axes, with $i \in \{1, 2, 3\}$

B | Materials

The following tables give an overview of the materials which where used in the calculations, as well as those that resulted from the simulation.

Material	elastic stiffness						electric permittivities		piezoelectric constant				Source
	c_{11}	c_{12}	c_{13}	c_{33}	c_{44}	c_{66}	κ_{11}	κ_{33}	e_{31}	e_{33}	e_{14}	e_{15}	
	GPa	GPa	GPa	GPa	GPa	GPa	pF/m	pF/m	C/m^2	C/m^2	C/m^2	C/m^2	
Cortical Bone	23.4	9.06	9.11	32.5	8.71	7.17	52.2	45.1	0.137	0.167	-1.89	0.375	[13, table 3]
Hydroxyapatite	142.47	52.67	52.67	142.47	44.9	44.9	108.2	99.61			0.606		[39]–[41]
Hydroxyapatite anisotropic	137	42.5	54.9	172	39.6	108.2		99.61			0.606		[41]–[43]
flourapatite	143.4	44.5	57.5	180.5	41.5	49.5							[44]
Dry collagen	11.7	5.1	7.1	17.9	3.3		13.55		0.0384	0.012	-1.069	0.594	[45], [46]
Salt water[1]	2.3006	2.3	2.3	0.0002	0.0002		619.8	619.8					[47], [48]

Table B.1: Used material parameters.

Bone materials	elastic stiffness						electric permittivities		piezoelectric constant			
	c_{11}	c_{12}	c_{13}	c_{33}	c_{44}	c_{66}	κ_{11}	κ_{33}	e_{31}	e_{33}	e_{14}	e_{15}
	GPa	GPa	GPa	GPa	GPa	GPa	pF/m	pF/m	C/m^2	C/m^2	C/m^2	C/m^2
wet collagen	4.69	3.24	3.61	8.53	0.93	0.73	44.86	353.04	0.0014	0.0049	-0.03	0.01
fibrils	8.2	4.76	5.24	16.86	2.22	1.72	59.52	257.12	0.01	0.19	-0.01	0.02
hydroxyapatite foam	51.64	17.87	17.87	51.64	16.89	16.89	205.9	197.5	0	0	0.3	0
extracellular bone matrix	20.3	8.86	8.86	32.17	7.12	5.72	112.76	229.1	0	0	0.08	0.01
extravascular bone material	19.6	8.58	8.6	30.87	6.84	5.51	117.4	233.78	0	0	0.08	0.01

Table B.2: Calculated material parameters of a human femur, as shown in chapter 5.

[1]The values for water are representing an isotonic salt concentration of 0.9%, homologous to body fluids.

C | Piezo-Eshelby tensor for anisotropic materials

For calculations with anisotropic matrix materials, which also occur when using the self-consistent homogenization scheme with inclusions featuring $\alpha \neq 1$, the calculations from section 4.2 can be applied, but with an anisotropic material as in Equation C.1 (stated in Voigt-notation here).

$$\mathbf{M}_{iJAb}^{aniso} = \begin{pmatrix} c_{11} & c_{12} & c_{13} & 0 & 0 & 0 & 0 & 0 & e_{31} \\ c_{21} & c_{22} & c_{23} & 0 & 0 & 0 & 0 & 0 & e_{32} \\ c_{31} & c_{32} & c_{33} & 0 & 0 & 0 & 0 & 0 & e_{33} \\ 0 & 0 & 0 & c_{44} & 0 & 0 & e_{14} & e_{24} & 0 \\ 0 & 0 & 0 & 0 & c_{55} & 0 & e_{15} & e_{25} & 0 \\ 0 & 0 & 0 & 0 & 0 & c_{66} & 0 & 0 & 0 \\ 0 & 0 & 0 & e_{14} & e_{15} & 0 & -\kappa_{11} & 0 & 0 \\ 0 & 0 & 0 & e_{24} & e_{25} & 0 & 0 & -\kappa_{22} & 0 \\ e_{31} & e_{32} & e_{33} & 0 & 0 & 0 & 0 & 0 & -\kappa_{33} \end{pmatrix} \tag{C.1}$$

According to Equation 4.3, the matrix $K_{MJ}(\vec{x})$ will result as in Equation C.2.

$$K_{MJ}(\vec{x}) = \begin{pmatrix} c_{11}\,{x_1}^2 + c_{66}\,{x_2}^2 + c_{44}\,{x_3}^2 & x_1\,x_2\,(c_{12} + c_{66}) & x_1\,x_3\,(c_{13} + c_{55}) & x_1\,x_3\,(e_{15} + e_{31}) + e_{25}\,x_2\,x_3 \\ x_1\,x_2\,(c_{21} + c_{66}) & c_{66}\,{x_1}^2 + c_{22}\,{x_2}^2 + c_{44}\,{x_3}^2 & x_2\,x_3\,(c_{23} + c_{44}) & x_2\,x_3\,(e_{24} + e_{32}) + e_{14}\,x_1\,x_3 \\ x_1\,x_3\,(c_{31} + c_{44}) & x_2\,x_3\,(c_{32} + c_{44}) & c_{44}\,{x_1}^2 + c_{55}\,{x_2}^2 + c_{33}\,{x_3}^2 & e_{15}\,{x_1}^2 + e_{24}\,{x_2}^2 + e_{33}\,{x_3}^2 \\ & & & +e_{14}\,x_1\,x_2 + e_{25}\,x_1\,x_2 \\ x_1\,x_3\,(e_{15} + e_{31}) + e_{25}\,x_2\,x_3 & x_2\,x_3\,(e_{24} + e_{32}) + e_{14}\,x_1\,x_3 & e_{15}\,{x_1}^2 + e_{24}\,{x_2}^2 + e_{33}\,{x_3}^2 & -k_{11}\,{x_1}^2 - k_{11}\,{x_2}^2 - k_{33}\,{x_3}^2 \\ & & +e_{14}\,x_1\,x_2 + e_{25}\,x_1\,x_2 & \end{pmatrix} \tag{C.2}$$

Inverting the matrix $K_{MJ}(\vec{x})$ and implying the needed geometry will yield the required Eshelby tensor as in section 4.4 and section 4.5.

Bibliography

[1] J. Wolff, *Das Gesetz der Transformation der Knochen*, German. Verlag von August Hirschwald, 1892, urn:nbn:de:hbz:38m:1-41917.

[2] A. Haynes and N. Russell, "Hematopoiesis," in *Principles of Molecular Medicine*, J. L. Jameson, Ed. Totowa, NJ: Humana Press, 1998, pp. 171–178, ISBN: 978-1-59259-726-0.

[3] L. D. Quarles, "Endocrine functions of bone in mineral metabolism regulation," *The Journal of Clinical Investigation*, vol. 118, no. 12, pp. 3820–3828, Dec. 2008.

[4] R. Florencio-Silva, G. R. da Silva Sasso, E. Sasso-Cerri, M. J. Simões, and P. S. Cerri, "Biology of bone tissue: Structure, function and factors that influence bone cells," *Hindawi Publishing Corporation*, vol. 2015, p. 421 746, 2015.

[5] Y. Mikuni-Takagaki, K Naruse, Y Azuma, and A Miyauchi, "The role of calcium channels in osteocyte function," *Journal of musculoskeletal & neuronal interactions*, vol. 2, pp. 252–5, Apr. 2002.

[6] G. Hastings and F. Mahmud, "Electrical effects in bone," *Journal of Biomedical Engineering*, vol. 10, no. 6, pp. 515 –521, 1988, ISSN: 0141-5425.

[7] S. Verbruggen, T. Vaughan, and L. Mcnamara, "Fluid flow in the osteocyte mechanical environment: A fluid-structure interaction approach," *Biomechanics and modeling in mechanobiology*, vol. 13, Apr. 2013.

[8] J. Green, S. Schotland, D. J. Stauber, C. R. Kleeman, and T. L. Clemens, "Cell-matrix interaction in bone: Type i collagen modulates signal transduction in osteoblast-like cells," *American Journal of Physiology-Cell Physiology*, vol. 268, no. 5, pp. C1090–C1103, 1995, PMID: 7762601.

[9] A. Gjelsvik, "Bone remodeling and piezoelectricity — i," *Journal of Biomechanics*, vol. 6, no. 1, pp. 69 –77, 1973, ISSN: 0021-9290.

[10] ——, "Bone remodeling and piezoelectricity — ii," *Journal of Biomechanics*, vol. 6, no. 2, pp. 187 –193, 1973, ISSN: 0021-9290.

[11] A. Bigham-Sadegh and A. Oryan, "Basic concepts regarding fracture healing and the current options and future directions in managing bone fractures," *International Wound Journal*, vol. 12, no. 3, pp. 238–247, 2015.

[12] V. Perschon, *Auswirkungen von Inaktivität auf Muskulatur und Knochen sowie Einfluß trainingsspezifischer Maßnahmen zur Vermeidung deadaptiver Veränderungen in Schwerelosigkeit*, ger. 2008.

[13] A. R. Aguiar, J. Bravo-Castillero, and U. P. da Silva, "Application of mori–tanaka method in 3–1 porous piezoelectric medium of crystal class 6," *International Journal of Engineering Science*, vol. 123, pp. 36 –50, 2018, ISSN: 0020-7225.

[14] A. Zaoui, "Continuum micromechanics: Survey," *Journal of Engineering Mechanics*, vol. 128, no. 8, pp. 808–816, 2002.

[15] A. Fritsch and C. Hellmich, "'universal' microstructural patterns in cortical and trabecular, extracellular and extravascular bone materials: Micromechanics-based prediction of anisotropic elasticity," *Journal of Theoretical Biology*, vol. 244, no. 4, pp. 597 –620, 2007, ISSN: 0022-5193.

[16] A. Solo, "Multidimensional matrix mathematics: Multidimensional matrix transpose, symmetry, antisymmetry, determinant, and inverse, part 4 of 6," *Lecture Notes in Engineering and Computer Science*, vol. 2185, Jun. 2010.

[17] Y. Mikata, "Determination of piezoelectric eshelby tensor in transversely isotropic piezoelectric solids," *International Journal of Engineering Science - INT J ENG SCI*, vol. 38, pp. 605–641, Apr. 2000.

[18] T. Michelitsch, H. Gao, and V. Levin, "Dynamic eshelby tensor and potentials for ellipsoidal inclusions," *Proceedings of the Royal Society London A, v.459, 863-890 (2003)*, vol. 459, Apr. 2003.

[19] C. Hellmich, J.-F. Barthélémy, and L. Dormieux, "Mineral–collagen interactions in elasticity of bone ultrastructure – a continuum micromechanics approach," *European Journal of Mechanics - A/Solids*, vol. 23, no. 5, pp. 783 –810, 2004, ISSN: 0997-7538.

[20] C. Hellmich and F.-J. Ulm, "Micromechanical model for ultrastructural stiffness of mineralized tissues," *Journal of Engineering Mechanics*, vol. 128, no. 8, pp. 898–908, 2002.

[21] S. Lees, P. F. Cleary, J. D. Heeley, and E. L. Gariepy, "Distribution of sonic plesio-velocity in a compact bone sample," *The Journal of the Acoustical Society of America*, vol. 66, no. 3, pp. 641–646, 1979.

[22] R. Zohar, "Signals between cells and matrix mediate bone regeneration," 2012.

[23] J. Jacob, N. More, K. Kalia, and G. Kapusetti, "Piezoelectric smart biomaterials for bone and cartilage tissue engineering," *BMC Springer - Inflammation and Regeneration*, vol. 52, Feb. 2018.

[24] K. Tanaka-Kamioka, H. Kamioka, H. Ris, and S.-S. Lim, "Osteocyte shape is dependent on actin filaments and osteocyte processes are unique actin-rich projections," *Journal of Bone and Mineral Research*, vol. 13, no. 10, pp. 1555–1568, 1998.

[25] D. L. Ypey, A. F. Weidema, K. M. Höld, A. Van Der Laarse, J. H. Ravesloot, A. Van Der Plas, and P. J. Nijweide, "Voltage, calcium, and stretch activated ionic channels and intracellular calcium in bone cells," *Journal of Bone and Mineral Research*, vol. 7, no. S2, S377–S387, 1992.

[26] J. Golowasch and F. Nadim, "Capacitance, membrane," in *Encyclopedia of Computational Neuroscience*, D. Jaeger and R. Jung, Eds. New York, NY: Springer New York, 2013, pp. 1–5, ISBN: 978-1-4614-7320-6.

[27] D. Carter and W. Hayes, "Bone compressive strength: The influence of density and strain rate," *Science (New York, N.Y.)*, vol. 194, pp. 1174–6, Jan. 1977.

[28] C Turner, T Wang, and D. Burr, "Shear strength and fatigue properties of human cortical bone determined from pure shear tests," *Calcified tissue international*, vol. 69, pp. 373–8, Jan. 2002.

[29] M. Minary-Jolandan and M.-F. Yu, "Nanoscale characterization of isolated individual type i collagen fibrils: Polarization and piezoelectricity," *Nanotechnology*, vol. 20, no. 8, p. 085 706, 2009.

[30] V. Thompson and N. Silva, "1 - structure and properties of enamel and dentin," in *Non-Metallic Biomaterials for Tooth Repair and Replacement*, ser. Woodhead Publishing Series in Biomaterials, P. Vallittu, Ed., Woodhead Publishing, 2013, pp. 3 –19, ISBN: 978-0-85709-244-1.

[31] J. Cuy, A. Mann, K. Livi, M. Teaford, and T. Weihs, "Nanoindentation mapping of the mechanical properties of human molar tooth enamel," *Archives of Oral Biology*, vol. 47, no. 4, pp. 281 –291, 2002, ISSN: 0003-9969.

[32] Y.-R. Zhang, W. Du, X.-D. Zhou, and H.-Y. Yu, "Review of research on the mechanical properties of the human tooth," *International Journal of Oral Science*, vol. 6, pp. 61–69, 2014.

[33] I. Spears, "A three-dimensional finite element model of prismatic enamel: A re-appraisal of the data on the young's modulus of enamel," *Journal of dental research*, vol. 76, pp. 1690–7, Nov. 1997.

[34] J. Reyes-Gasga, M. Galindo-Mentle, E. Brès, N. Vargas-Becerril, E. Orozco, A. Rodríguez-Gómez, and R. García-García, "Detection of the piezoelectricity effect in nanocrystals from human teeth," *Journal of Physics and Chemistry of Solids*, vol. 136, p. 109 140, 2020, ISSN: 0022-3697.

[35] M. Goldberg, A. Kulkarni, M. Young, and A. Boskey, "Dentin: Structure, composition and mineralization," *PubMed*, vol. 3, pp. 711–735, 2012.

[36] J. Kinney and G. Marshall, "The mechanical properties of human dentin: A critical review and re-evaluation of the dental literature," *Critical reviews in oral biology and medicine : an official publication of the American Association of Oral Biologists*, vol. 14, pp. 13–29, Feb. 2003.

[37] H. Athenstaedt, "Pyroelectric and piezoelectric behaviour of human dental hard tissues," *Archives of Oral Biology*, vol. 16, no. 5, pp. 495 –501, 1971, ISSN: 0003-9969.

[38] A. R. Liboff and M. H. Shamos, "Piezoelectric effect in dentin," *Journal of Dental Research*, vol. 50, no. 2, pp. 516–516, 1971, PMID: 5290902.

[39] M. L. Dunn, "Electroelastic green's functions for transversely isotropic piezoelectric media and their application to the solution of inclusion and inhomogeneity problems," *International Journal of Engineering Science*, vol. 32, no. 1, pp. 119 –131, 1994, ISSN: 0020-7225.

[40] R. B. Ashman and J. Y. Rho, "Elastic modulus of trabecular bone material," *Journal of Biomechanics*, vol. 21, no. 3, pp. 177 –181, 1988, ISSN: 0021-9290.

[41] S. Lang, S. Tofail, A. Gandhi, M. Gregor, C. Wolf-Brandstetter, J. Kost, S. Bauer, and M. Krause, "Pyroelectric, piezoelectric, and photoeffects in hydroxyapatite thin films on silicon," *Applied Physics Letters*, vol. 98, pp. 123 703–123 703, Mar. 2011.

[42] S. A. M. Tofail, D. Haverty, F. Cox, J. Erhart, P. Hána, and V. Ryzhenko, "Direct and ultrasonic measurements of macroscopic piezoelectricity in sintered hydroxyapatite," *Journal of Applied Physics*, vol. 105, no. 6, p. 064 103, 2009.

[43] J. Katz and K. Ukraincik, "On the anisotropic elastic properties of hydroxyapatite," *J Biomech 1971*, 1971.

[44] H. S. Yoon and R. E. Newnham, "Elastic properties of fluorapatite," *American Mineralogist*, vol. 54, no. 7-8, pp. 1193–1197, Aug. 1969, ISSN: 0003-004X.

[45] S. Cusack and A. Miller, "Determination of the elastic constants of collagen by brillouin light scattering," *Journal of Molecular Biology*, vol. 135, no. 1, pp. 39 –51, 1979, ISSN: 0022-2836.

[46] C. Galassi, M. Dinescu, K. Uchino, and M. Sayer", *Piezoelectric Materials: Advances in Science, Technology and Applications*. Feb. 1, 2000, ch. 2, ISBN: 9780792362135.

[47] Y. J. Yoon and S. C. Cowin, "The elastic moduli estimation of the solid-water mixture," *International Journal of Solids and Structures*, vol. 46, no. 3, pp. 527 –533, 2009, ISSN: 0020-7683.

[48] J. B. Hasted, D. M. Ritson, and C. H. Collie, "Dielectric properties of aqueous ionic solutions. parts i and ii," *The Journal of Chemical Physics*, vol. 16, no. 1, pp. 1–21, 1948.